FEDERAL UNIVERSITY OF ITAJUBÁ

GRADUATE PROGRAM IN MATERIALS SCIENCE AND ENGINEERING

JÚLIO GABRIEL DE FALCO MANUEL

A COMPUTATIONAL STUDY ON POWER LAW AND WEIBULL MODELS APPLIED TO MAGNETORHEOLOGICAL FLUIDS

ITAJUBÁ/MG

2024

JÚLIO GABRIEL DE FALCO MANUEL

A COMPUTATIONAL STUDY ON POWER LAW AND WEIBULL MODELS APPLIED TO MAGNETORHEOLOGICAL FLUIDS

Thesis submitted to the Examining Committee from the Federal University of Itajubá to obtain a master's degree in Materials Science and Engineering.

Supervisors:

Prof. Dr. Antonio José Faria Bombard
Prof. Dr. Pedro Paulo Balestrassi

ITAJUBÁ/MG

2024

This work is dedicated to my friends, family, and, especially, my mother: I wouldn't have made it this far without her.

ACKNOWLEDGEMENTS

As I finish writing this thesis, I'd like to thank all who helped me through these difficult times:

To God, for all the lessons and opportunities.

To my family and girlfriend, for the never-ending support and encouragement.

To my dear friends: Gabriel Lamberti, Gabriel Siqueira Ferreira, Lucas Eduardo, Lucas Prado, Luiz Guilherme Faria, Rafael Almeida and Samuel Siqueira Ferreira.

To my mentors: Dr. Antonio José Faria Bombard and Dr. Eric R. Weeks.

To the great research opportunities provided by both the Federal University of Itajubá (Itajubá, MG, Brazil) and Emory University (Atlanta, GA, USA).

"For small creatures such as we, the vastness is bearable only through love."

(Carl Sagan)

ABSTRACT

Magnetorheological fluids (MRFs) are smart materials of increasing interest in research and industry due to their versatility in mechanical and mechatronic systems. As main rheological features, MRFs must present low viscosity in the absence of a magnetic field (0.1 - 1.0 Pa.s) and high yield stress (50 - 100 kPa) when magnetized in order to optimize the magnetorheological effect, which is responsible for its most important properties. These properties, in turn, are directly influenced by the composition, volume fraction (concentration), size, and size distribution (polydispersity) of the suspended particles, the latter being one of the most important factors in improving their quality. As is well known in the literature, widening the size distribution of the solid phase increases the maximum packing fraction and reduces the viscosity of concentrated suspensions. Therefore, by carefully adjusting the polydispersity, it is possible to increase the magnetorheological effect of concentrated MRFs. However, there is no known analytical model to calculate the so-called packing efficiency of particulate materials, and a numerical approach is often necessary. In this context, many functions can be used in these approximations, and this work aims to study via simulations three common models from science and engineering: the Andreasen-Andersen distribution, the Dinger-Funk distribution (modified Andreasen-Andersen), and the Weibull distribution. Simulations in 1D and 3D were carried out to compute the packing fractions, and their data were compared. The simulation results show that when the distribution modulus of the Dinger-Funk distribution is $q \approx 0.5$, there is a maximum packing fraction that should lower the relative viscosity. Also, the results show that by widening the particle size distribution, it is possible to get an even greater polydispersity of the solid phase. These data suggest that it may be possible to optimize the viscosity of MRFs by carefully adjusting the size distribution, paving the way for preparing MRFs with a stronger magnetorheological effect.

Keywords: Magnetorheological Fluid; Carbonyl Iron Powder; Polydispersity; Simulations; Random Close Packing; Power Law; Weibull distribution.

LIST OF FIGURES

LIST OF TABLES

LIST OF EQUATIONS

LIST OF ABBREVIATIONS

CDF   Cumulative Distribution Function

CIP   Carbonyl Iron Powder

ERF   Electrorheological Fluid

LALLS   Low-Angle Laser Light Scattering

MRF   Magnetorheological Fluid

PAO-2   Polyalphaolefin

PDF   Probability Density Function

PSD   Particle Size Distribution

$D_{4,3}$ Volume-Weighted Mean (De Brouckere Mean Diameter)

$D_{3,2}$ Surface-Weighted Mean (Sauter Mean Diameter)

SUMMARY

1 INTRODUCTION

Magnetorheological fluids (MRF) are smart materials that undergo a rapid and reversible transition from the liquid state to a quasi-solid state when exposed to an external magnetic field, modifying many of its rheological properties, such as viscoelasticity, plastic viscosity, yield stress, among others [1–3].

This transition, the so-called magnetorheological effect [4], makes the MRF extremely versatile materials, especially when dealing with mechanical systems that need vibration or torque control, such as dampers, brakes, and clutches [1, 5]. Furthermore, recent research indicates that MRFs are also viable options in high-precision polishing [6], robotics [7] (mechatronics), and even in the construction of devices for biomedical applications such as actuators in upper limb rehabilitation [8] and hydraulic actuation systems in surgeries [9].

This versatility is directly linked to the practicality of the magnetorheological effect: the magnetization of the suspended particles allows one to control the fluid's viscosity. By applying an external magnetic field to the fluid, each particle quickly becomes a dipole and starts interacting with adjacent ones. These attractive interactions create chain-like structures, which are aligned in the direction of the magnetic field, as illustrated in Figure 1 [1, 2, 4, 10]:
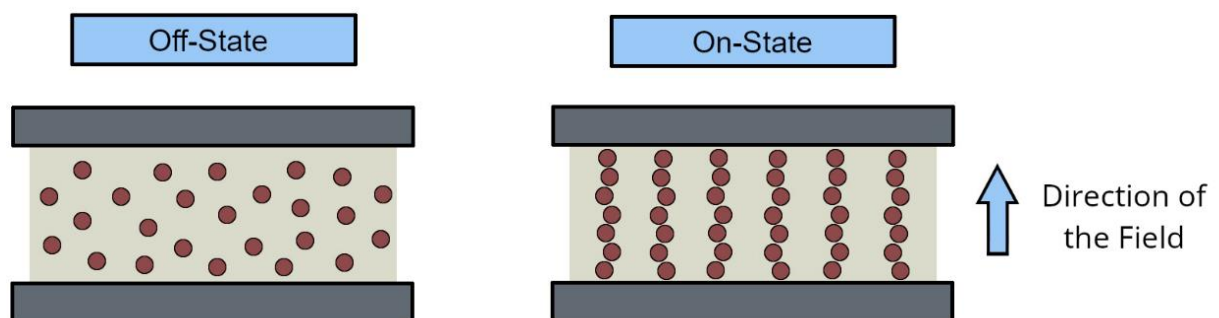
Figure 1 - The magnetorheological effect. The application of an external magnetic field generates chain-like structures parallel to the field lines. Source: Author, 2024.

The chain-like structures create resistance to flow, strengthening the suspension and increasing its viscosity. This resistance is directly related to the magnitude of the dipolar interactions, and these are influenced by the strength of the external magnetic field together with the volume fraction (concentration), magnetic properties, and shape of the suspended particles [2, 4, 11].

The composition of MRF is characterized by its simplicity: there is a suspended solid phase in the form of magnetizable particles (typically up to 50% of the volume, with a usual size of 0.1 – 10 μm) and a carrier liquid. For the solid-phase formulation, both ferrimagnetic materials (such as magnetite and chromium dioxide) and ferromagnetic materials (such as nickel, cobalt, iron, and carbonyl iron powder) can be used, with carbonyl iron powder being the most common choice due to its spheroidal shape and high saturation magnetization.

As for the carrier liquid, typical options include mineral or vegetable oils, synthetic or silicone oils, polyesters, polyethers, hydrocarbons, water, and ionic liquids [1, 10, 12, 13]. The liquid must have a wide operable temperature range [5] (−40 to 150 ℃, at least), be chemically inert (non-corrosive and non-reactive), show low vapor pressure and, preferably, be non-toxic.

Many patents also include surfactants and thixotropic additives in their composition to avoid agglomeration of the particles, slow their sedimentation, and control the fluid's viscosity. It is clear, therefore, that the formulation of an MRF is extremely dependent on the desired applications [2, 5, 10, 12].

Over the last few decades, much research has been carried out to improve the quality of these fluids, as well as to optimize the magnetorheological effect under different conditions. As ideal properties, an MRF should have low viscosity in the absence of field (off-state), and high viscosity and yield stress in the presence of field (on-state) [1, 2, 11, 14].

In this context, many studies indicate that the size and size distribution of the magnetic particles are important factors in manipulating these properties [3, 11, 14]. Since the work of Farris [15], it has been known that using bimodal, trimodal, or tetramodal particle populations can substantially reduce the relative viscosity of any suspension while also increasing its concentration.
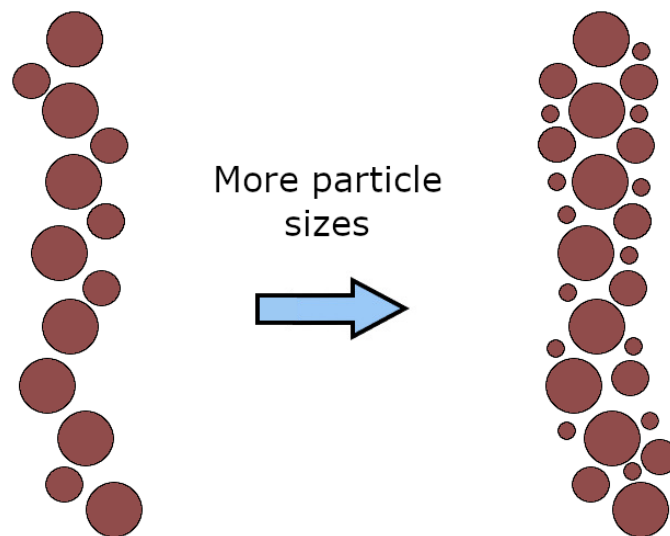
Figure 2 - By using many sizes of particles, one can greatly increase the concentration of the solid phase and reduce the relative viscosity of the suspension. Source: Author, 2024.

The so-called "Farris effect" (illustrated in Figure 2) becomes increasingly large at concentrations above 50 vol% and is extremely useful for adjusting the rheological properties of an MRF. For this reason, much research has been done in this area, and works such as Foister [16] pioneered (to the best of our knowledge) in patenting MRF based on bimodal mixtures.

To optimize the Farris effect, two parameters are key: (1) the size ratio between the particle sizes and (2) the amounts of particles and the particle size distributions used to prepare the suspension. For populations with the same median size and at fixed volume fractions, it is widely recognized that the broader their particle size distributions, the lower their viscosity will be [15, 17, 18, 19]. However, for most suspensions, including magnetorheological fluids and electrorheological fluids (ERF), the Farris effect is only noticeable in fractions well above 20 vol%; that is, it is only relevant in concentrated suspensions.

One must take care when dealing with concentrated suspensions, though: it is well reported in the literature that the viscosity of any dispersion increases dramatically by increasing the volume fraction of the solid phase. Therefore, the Farris effect must be carefully adjusted to maximize the magnetorheological effect: the viscosity should be as low as possible and the concentrations as high as possible.

In this context, it is also well known that a suspension's relative viscosity is dependent on the packing of its particles. This packing, in turn, is strictly related to their particle size distribution. To further delve into this topic, we must detail some fundamental concepts in particle size analysis and rheology, starting with the definition of polydispersity.

When analyzing particulate materials in detail, especially dense suspensions, one can easily see that they are seldom monodisperse; that is, the particles rarely show the same size. Most of the time, these particles will have different sizes and shapes, being, therefore, polydisperse. This is illustrated in Figure 3:
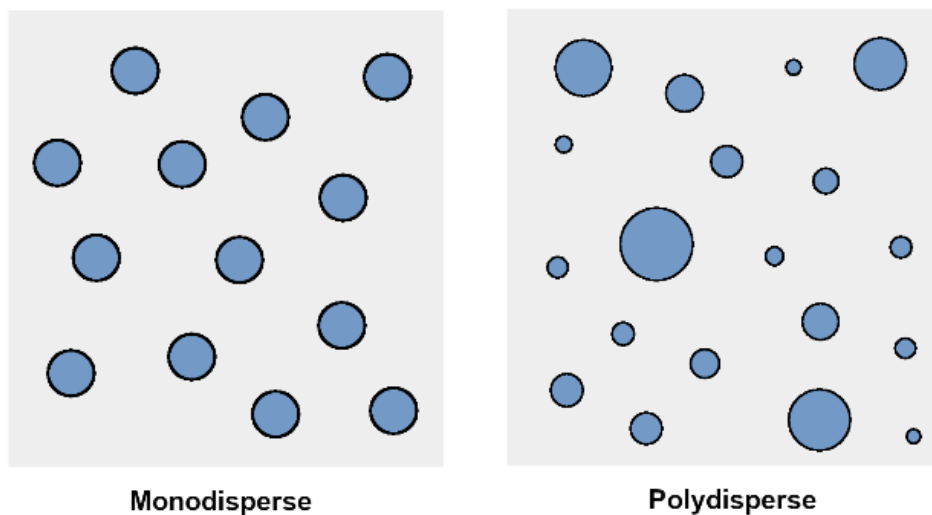
Figure 3 - Monodisperse and polydisperse particles. Source: Author, 2024.

These variations in size can be described by using frequency distributions, the so-called particle size distributions (PSD) [18, 20]. A particle size distribution (illustrated in Figure 4) is a probability density function that expresses, in detail, the polydispersity of the analyzed material, that is, how different the particle sizes in a system are. Many statistical distributions can be used to model a size distribution, and along with important mathematical tools, such as mode, mean, median, and standard deviation, these variations in particle sizes can be studied and quantified [21, 22].
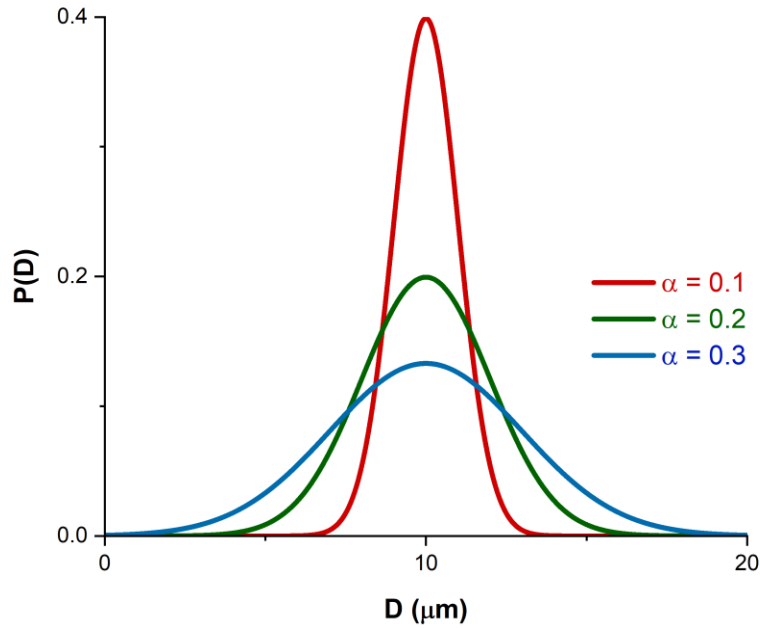
Figure 4 – A gaussian particle size distribution: the greater its width, the greater its polydispersity. Source: Author, 2024.

A key piece in particle size analysis, size distributions are critical in several areas of science and engineering, often appearing in soil and aerosol studies, mining, and even in the food industry. Polymers and resins [23], paints [24], and drugs [25] are directly influenced by the size, quantity, and morphology of their particles. A list of the most common particle size distributions is given in Appendix A for reference.

Several statistical parameters may prove useful when describing a PSD. Among them, the polydispersity index α is the one that stands out the most: a direct measure of polydispersity, the higher its value, the greater the discrepancy in particle sizes. Its definition is given in equation 1 [18, 26]:

$$\alpha = \frac{\sqrt{\langle \Delta D^2 \rangle}}{\langle D \rangle} \ , \tag{1}$$

where D is the particle diameter, $\langle D \rangle$ is the mean, $\langle D^n \rangle = \int_0^\infty D^n P(D) dD$ is the n-th moment of D, $\Delta D = D - \langle D \rangle$ and $\langle \Delta D^n \rangle = \int_0^\infty \Delta D^n P(D) dD$.

It is worth noting that α takes many different forms depending on the probability distribution $p(D)$ that we choose. However, its meaning is always the same: a measure of the spread of a variable around the mean [18]. As for the width of the distribution, one can define another important parameter, the span, to analyze it [27, 28]:

$$Span = \frac{D_{90} - D_{10}}{D_{50}} \, , \tag{2}$$

where D_{90} is the particle size corresponding to the 90th percentile, D_{10} is the size of the 10th percentile and D_{50}, the median size.

The span is also closely related to the variations in particle sizes and works similarly to α: the higher its value, the greater the polydispersity. The shape of a PSD, in turn, is determined by the coefficients of skewness S and kurtosis K, respectively. Their definitions are given below [26, 29]:

$$S = \frac{\langle \Delta D^3 \rangle}{\langle \Delta D^2 \rangle^{3/2}} \, , \tag{3}$$

$$K = \frac{\langle \Delta D^4 \rangle}{\langle \Delta D^2 \rangle^2} \, . \tag{4}$$

In general, the skewness measures the distortion of a frequency distribution, that is, how much it deviates from symmetry: $S > 0$ indicate a larger fraction of small particles, $S < 0$ indicates a larger fraction of large particles, and $S = 0$ indicates a symmetric distribution [29, 30].

Kurtosis, in turn, is commonly interpreted as a measure of peakedness: a positive value generates distributions with higher peaks and larger tails, while negative values generate more flattened curves, with smaller tails [30, 31]. Together, all these concepts can be used to properly describe the variability of a particulate material.

Another important (and often overlooked) detail is that there are several ways to describe the same particle size distribution according to the physical property that is measured [20]. For example, if we simply count the frequency of each class of particles in a system, we obtain what is called a number-weighted size distribution.

However, if we employ a laser technique such as the Low-Angle Laser Light Scattering (LALLS) to analyze our particles, we obtain a measure of the total volume of each class of particles, creating a volume-weighted distribution. To convert between each type, one can use the formula below [20]:

$$q_r(D) = \frac{D^{r-t}}{\int_{D_{min}}^{D_{max}} D^{r-t} q_t(D) dD} \, q_t(D) \; , \tag{5}$$

where q_t is our original probability distribution and q_r is our converted distribution. The parameters r and t are chosen according to the conversion and can assume the values 0, 1, 2, and 3 for number, length, surface, and volume distributions, respectively. For example, if we want to convert a number distribution to a volume distribution, we use $t = 0$ and $r = 3$ [20]. However, one must take care when transforming between distributions, because some statistical information is always lost, leading to conversion errors.

By reviewing the literature on particulate materials, especially regarding civil engineering, one may come across two important volume-based models: the Andreasen-Andersen model [32], which is based on the work of Furnas [33], Fuller and Thompson [34], and the Dinger-Funk model [35], which is a modified version of the Andreasen and Andersen equation. Both models were developed to explain the granulometry of cement and concrete and their cumulative distributions (CDF) are defined as follows:

1. Andreasen-Andersen model [32]:

$$F(D) = \left(\frac{D}{D_{max}}\right)^q \qquad 0 \leq D \leq D_{max} \; ; \quad q > 0 \; ; \; D_{max} > 0 \quad , \tag{6}$$

where D is the i-th particle size, D_{Max} is the largest particle size, and q is the distribution modulus, an empirically determined exponent.

2. Dinger-Funk model (modified Andreasen-Andersen) [35]:

$$F(D) = \frac{D^q - D_{min}^q}{D_{max}^q - D_{min}^q} \qquad D_{min} \le D \le D_{max}\,;\quad q \ne 0,\ D_{min}, D_{max} > 0 \quad, \quad (7)$$

where D is the particle size, D_{min} is the minimum particle size, D_{max} is the largest particle size and q is the distribution modulus. Both models, which are special types of power laws, found many applications in industrial processes, especially regarding the production of ceramics and milling [35].

Another important model from particle size analysis is the so-called Rosin-Rammler distribution [36]. Originally developed to analyze powdered coal, this volume-weighted function is defined as follows [37]:

$$F(x) = 1 - e^{\left(-\frac{x}{x_0}\right)^n}\,, \qquad (8)$$

where n and x_0 are constants that describe the material uniformity and the "characteristic particle size", respectively.

Despite being empirically determined, Weibull [38] showed that this function belongs to a greater family of functions that are applicable to a wide range of problems in science and engineering [39, 40, 41]. For this reason, it is now known as the Weibull distribution. A more general formula for this distribution is given below:

$$F(D) = 1 - e^{-\left(\frac{D-a}{b}\right)^c} \qquad D \ge a;\ a, b, c > 0 \,, \qquad (9)$$

where a, b, and c are the location, scale and shape parameters, respectively.

In addition to describing particle sizes, these models' contributions may be extended even further: there is a well-known relationship between viscosity and packing efficiency. In fact, if we know the maximum packing fraction of this arrangement, we can estimate the viscosity of a suspension prepared with these particles.

To do so, we may use some well-established models from both rheology and particle size analysis, such as the Maron, Pierce, Kitano, and Quemada equation [42, 43, 44]:

$$\eta_r = \frac{\eta_{suspension}}{\eta_{pure\,fluid}} = \left(1 - \frac{\phi}{\phi_{max}}\right)^{-2} \quad , \tag{10}$$

where η_r is the relative viscosity of the MR fluid, ϕ is the volume fraction of the solid phase, and ϕ_{max} is the maximum packing fraction.

A more complete version of this model is given by Krieger and Dougherty [45], which considers a shape-dependent factor called intrinsic viscosity $[\eta]$:

$$\eta_r = \left(1 - \frac{\phi}{\phi_{max}}\right)^{-[\eta]\phi_{max}} \quad . \tag{11}$$

Naturally, since magnetorheological fluids are a special type of suspension, an extension of these concepts to magnetorheology would prove most useful: by optimizing the packing efficiency of the solid phase, one can effectively reduce the off-state viscosity and increase the magnetorheological effect.

However, we first need to know both the size distribution and the packing efficiency of the solid phase, that is, its maximum packing fraction. Unfortunately, up to now, there is no known analytical formula to calculate this parameter directly, and we need to either estimate the maximum packing fraction by empirically analyzing the material's viscosity vs. solid fraction curve [46] or use computer simulations [26, 47].

In a previous work [48], our research group successfully investigated, both experimentally and via simulations, the influence of polydispersity on the properties of concentrated magnetorheological fluids. In fact, we showed that by increasing the polydispersity of the solid phase, the maximum packing fraction increases, optimizing the magnetorheological effect.

This work is an extension of our previous paper, and we aim to study both the power law and Weibull models and compare their packings via simulations in 1D and 3D. At first, a review of power laws and Weibull distributions is performed, followed by an extensive discussion of the methodology. Then, the results are presented and discussed. Finally, the work is concluded, and proposals for future research are presented.

2 OBJECTIVES

2.1 GENERAL OBJECTIVES

Study the power law and Weibull models in the context of particle simulations to determine if these models can potentially be used to improve the magnetorheological effect of MRF.

2.2 SPECIFIC OBJECTIVES

Describe the most common packing models and how they can be used in the context of magnetorheology.

Develop a fast and reliable algorithm to analyze histograms of particle sizes, allowing one to quickly estimate the maximum packing fraction of the solid phase of dispersions.

3 POWER LAWS

Power law (or scaling law) is a generic term used to describe a non-linear relationship between two variables such that [49, 50]:

$$y = ax^q \quad , \tag{12}$$

where a and q are constants that describe, respectively, the width of the scaling relationship and the magnitude of the power law.

There are many types of power laws in science and statistics, depending on the constants utilized. For example, the so-called Pareto distribution (Zipf's law) is defined as follows [51, 52]:

$$p(X) = \frac{q}{X}\left(\frac{X_{min}}{X}\right)^q \qquad X_{min} \leq X < \infty, \; X_{min} > 0, \; q > 0 \quad , \tag{13}$$

$$F(X) = 1 - \left(\frac{X_{min}}{X}\right)^q \qquad X_{min} \leq X < \infty, \; X_{min} > 0, \; q > 0 \quad , \tag{14}$$

where X is a random variable, X_{min} is the scale parameter, and q is the shape parameter.

Another important variation that will be thoroughly analyzed throughout this thesis is simply known as "power function distribution". It is defined as [52]:

$$p(X) = \frac{q}{X}\left(\frac{X}{X_{max}}\right)^q \quad 0 \leq X \leq X_{max}, \quad X_{max} > 0, \quad q > 0 \quad , \tag{15}$$

$$F(X) = \left(\frac{X}{X_{max}}\right)^q \quad 0 \leq X \leq X_{max}, \quad X_{max} > 0, \quad q > 0 \quad , \tag{16}$$

where X is the random variable, X_{max} is the scale parameter, and q is the shape parameter. Notice that equations 13 and 15 are closely related: the power function distribution is just the inverse transformation of the Pareto distribution [53].

To better characterize the "power function distribution", we can use the following statistical parameters [52]:

Table 1 – Properties of the power function distribution

Parameters	Random Variable x, shape parameter q, scale parameter x_{max}
Range	$0 \leq x \leq x_{max}$
PDF	$f(x) = \dfrac{q x^{q-1}}{x_{max}^{q}}$
Mean	$\dfrac{x_{max}\, q}{q + 1}$
Mode	$\begin{cases} x_{max}, & if\ q > 1 \\ 0, & if\ q < 1 \end{cases}$
Median	$\dfrac{x_{max}}{2^{1/q}}$
Variance	$\dfrac{x_{max}^{2}\, q}{(q + 2)(q + 1)^{2}}$
Coefficient of Variation (Polydispersity Index)	$[q(q + 2)]^{-1/2}$
Skewness	$\dfrac{2(1 - q)(2 + q)^{\frac{1}{2}}}{q^{1/2}(3 + q)}$
Kurtosis	$\dfrac{3(q + 2)[2(q + 1)^{2} + q(q + 5)]}{q(q + 3)(q + 4)}$

Power laws are extremely common in nature and can be used to model a vast range of phenomena, such as the growth of city populations, the size of earthquakes, and the frequency at which words are used in human languages [51]. They are also closely related to fractals [54], showing the important property of scale-invariance, that is, $f(\lambda x) \propto f(x)$ for every value of λ [50]. The Andreasen-Andersen model and the Dinger-Funk model, extensively described in the following sections, are both power law models or power law-like models.

3.1 THE ANDREASEN-ANDERSEN MODEL

In 1907, Fuller and Thompson started to study the packing efficiency of concrete, mixing several populations of particles to obtain the densest possible configuration [35]. In 1928, Furnas [33] conducted similar research: using a series of regular sieves, he noted that the amounts of particles needed to "build" a cumulative size distribution followed a geometric progression; in other words, the ratio between the weights of two consecutive screens was always constant [33].

Naturally, both theories were quickly adopted to study packings of particles [35]. In this context, aiming to extend these models even further, Andreasen and Andersen [32] proposed their own empirical model, which is based on a power law. From equation 6, we know that their model is defined as follows:

$$CDF = \left(\frac{D}{D_{max}}\right)^q \qquad 0 \leq D \leq D_{max}, \quad D_{max} > 0, \quad q > 0 \quad ,$$

where D is the i-th particle size, D_{max} is the greatest particle size, and q is the distribution modulus, an empirically determined exponent. Also, recall from equation 16 that:

$$F(X) = \left(\frac{X}{X_{max}}\right)^c \qquad 0 \leq X \leq X_{max}, \quad X_{max} > 0, \quad c > 0 \quad .$$

So, it is straightforward to see that the Andreasen-Andersen model follows a power law distribution (more specifically, a power function distribution) with $c = q$ and $X_{max} = D_{max}$.

After extensive experimentation, Andreasen and Andersen advised that the exponent q should be between $1/3 < q < 1/2$ for better packing efficiency of concrete and mortar formulations. Also, by letting $q \to \infty$, we get more and more closer to a monodisperse arrangement.

3.2 THE DINGER-FUNK MODEL

Despite its usefulness, the Andreasen-Andersen model raised many objections and was overlooked by their peers for several years. This happened not only because their model was empirical but because it had an important limitation: it admitted the existence of infinitely small particles in the system.

This limitation would be solved only fifty years later when Dinger and Funk [35] proposed a modified version of the Andreasen-Andersen model. From equation 7, we know that their model is defined as follows:

$$CDF(D) = \frac{D^q - D_{min}^q}{D_{max}^q - D_{min}^q} \qquad D_{min} < D < D_{max} \;\; ; \;\; D_{min}, D_{max}, q \neq 0 \;\; ,$$

where D is the i-th particle size, D_{min} is the minimum particle size, D_{max} is the maximum particle size, and q is the distribution modulus, which was obtained via simulations. For better packing efficiency, that is, the densest possible configuration, Dinger and Funk recommended that $q = 0.56$ in 2D systems and $q = 0.37$ in 3D systems.

An interesting result of this model is that the exponent q now has a well-defined physical meaning: it measures the availability of contiguous volume that the particles can occupy. When $q = 0.37$ (the optimum value), the contiguous space is ideal, and the porosity goes to zero at the highest possible rate. When $q <$ optimum, the arrangement's porosity (void fraction) goes to zero by adding smaller particles. Finally, when $q >$ optimum, the porosity never reaches zero and eventually settles into a fixed value if we add more finer particles [35].

The derivation of the Dinger and Funk model is brilliantly described using an empirical approach in their book. However, it is also possible to derive their model by truncating the power law distribution. According to Tokmachev [55], a doubly truncated probability density function is defined as:

$$t(x) = \frac{p(x)}{\int_{x_{min}}^{x_{max}} p(x)\,dx} \qquad x_{min} \leq x < x_{max}, \ x_{min} > 0, \ x_{max} > x_{min} \ , \qquad (17)$$

where $p(x)$ is our original probability density function.

Integrating equation 17, we can quickly obtain the doubly truncated cumulative distribution:

$$T(x) = \frac{\int_{x_{min}}^{x} p(t)\,dt}{\int_{x_{min}}^{x_{max}} p(x)\,dx} \qquad x_{min} \leq x < x_{max}, \ x_{min} > 0, \ x_{max} > x_{min} \ . \qquad (18)$$

Combining equations 15 and 17, we find that the doubly truncated power law is given by:

$$t(x) = \frac{cx^{c-1}}{x_{max}^{c} - x_{min}^{c}} \qquad . \qquad (19)$$

Integrating, we get:

$$T(x) = \frac{x^{c} - x_{min}^{c}}{x_{max}^{c} - x_{min}^{c}} \qquad . \qquad (20)$$

Comparing equations 7 and 20, it is straightforward to see that the Dinger-Funk model is, in fact, a doubly truncated power function distribution with $c = q$, $x_{max} = D_{max}$, and $x_{min} = D_{min}$. Therefore, the Andreasen-Andersen and Dinger-Funk models are not only closely related but also have a well-defined mathematical behavior: the power law.

4 WEIBULL DISTRIBUTION

Originally identified by Fréchet [56] in 1927 and extensively studied by Weibull [38], the Weibull distribution is one of the most common models when analyzing non-normal data. A powerful tool in several areas of science and engineering, the Weibull distribution can also be utilized to model particle size distributions [36, 57, 58, 59].

Described by three main parameters, location (a), scale (b), and shape (c), the Weibull distribution (illustrated in Figure 5) encompasses a family of versatile and flexible functions that may be used to describe many types of distributions, whether they are approximately symmetrical or skewed [39, 40, 52]. Its number-weighted definition is given below:

$$p(D) = \frac{c}{b}\left(\frac{D-a}{b}\right)^{c-1} e^{-\left(\frac{D-a}{b}\right)^{c}} \qquad x \geq a;\ a,b,c > 0 \quad , \tag{21}$$

where D is the i-th diameter of a particle.
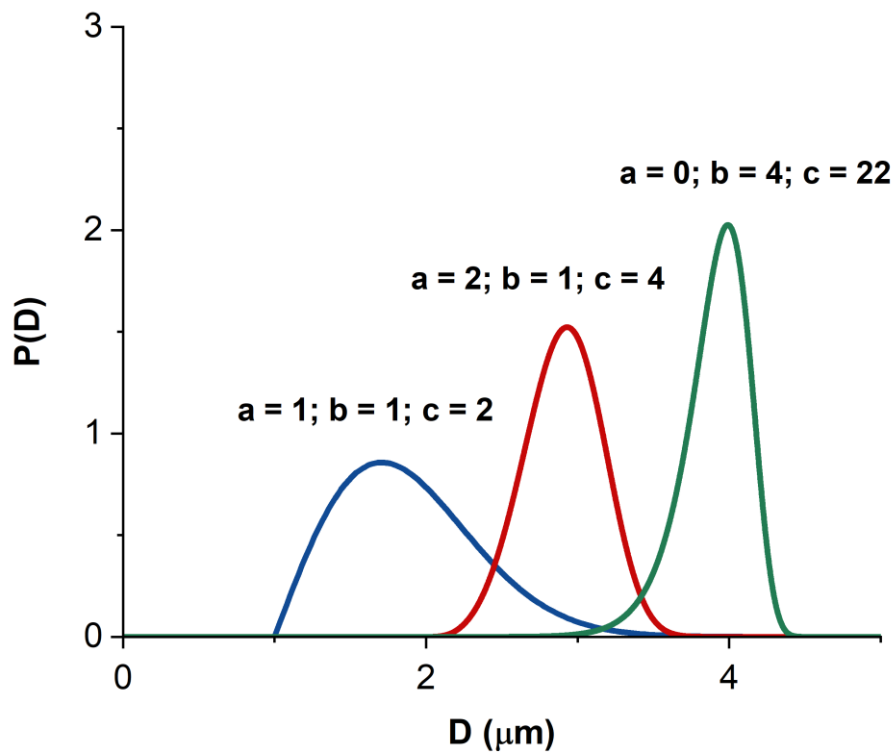
Figure 5 - Weibull distributions with variable parameters. Source: Author, 2024.

The main properties of this distribution are presented in table 2 [39, 40, 41, 52]:

Table 2 – Properties of a Weibull distribution

Parameters	Random Variable x, Location Parameter (a), Scale Parameter (b) and Shape Parameter (c)
Range	$x \geq a;\ a, b, c > 0$
PDF	$f(x) = \dfrac{c}{b}\left(\dfrac{x-a}{b}\right)^{c-1} e^{-\left(\frac{x-a}{b}\right)^{c}}$
Mean	$E(X) = a + b\Gamma(1 + 1/c)\ ‡$
Mode	$Mode(x) = \begin{cases} a + b(1 - 1/c)^{1/c}, & c \geq 1 \\ a, & 0 < c \leq 1 \end{cases}$
Median	$Med(x) = a + b(ln2)^{1/c}$
Variance	$Var(x) = b^2\{\Gamma(1 + 2/c) - [\Gamma(1 + 1/c)]^2\}$
Coefficient of Variation (Polydispersity Index)	$\alpha = \dfrac{b\{\Gamma(1 + 2/c) - [\Gamma(1 + 1/c)]^2\}^{1/2}}{a + b\Gamma(1 + 1/c)}$
Skewness	$S = \dfrac{\Gamma\left(1 + \frac{3}{c}\right) - 3\Gamma\left(1 + \frac{2}{c}\right)\Gamma\left(1 + \frac{1}{c}\right) + 2\left[\Gamma\left(1 + \frac{1}{c}\right)\right]^3}{\left\{\Gamma\left(1 + \frac{2}{c}\right) - \left[\Gamma\left(1 + \frac{1}{c}\right)\right]^2\right\}^{3/2}}$
Kurtosis	$K = \dfrac{\Gamma\left(1 + \frac{4}{c}\right) - 4\Gamma\left(1 + \frac{3}{c}\right)\Gamma\left(1 + \frac{1}{c}\right) + 6\Gamma\left(1 + \frac{2}{c}\right)\left[\Gamma\left(1 + \frac{1}{c}\right)\right]^2 - 3\left[\Gamma\left(1 + \frac{1}{c}\right)\right]^4}{\left\{\Gamma\left(1 + \frac{2}{c}\right) - \left[\Gamma\left(1 + \frac{1}{c}\right)\right]^2\right\}^2}$

‡ Where $\Gamma(x)$ is the gamma function of x, defined as: $\Gamma(x) = \int_0^\infty t^{x-1} e^{-t} dt.$

Since the Weibull distribution was originally employed to analyze coal slurries [36], it is also a suitable candidate for describing the solid phase of magnetorheological fluids. For the sake of simplicity, however, in this study, we will only analyze the behavior of the number-weighted Weibull distribution since it is easier to implement in the packing algorithms. Then, we will analyze how well this model can estimate the packing fraction of an arrangement of spherical particles.

Now that all models have their statistics well described, it should be easier to apply them in the context of magnetorheology. Recall from equations 10 and 11 that there is a well-defined relationship between the packing efficiency (which is controlled by the particle size distribution) and the relative viscosity of a suspension. If we somehow develop a simulation method to calculate this packing efficiency, we may be able to optimize the properties of future formulations of magnetorheological fluids. These simulation methods will be described in the following sections.

5 METHODOLOGY

By reviewing the literature, we can find several algorithms that may be used to estimate the maximum packing fraction of an arrangement of particles [60, 61, 62]. Among them, two stand out: the 1D algorithm developed by Farr and Groot [63] and the 3D algorithm by Desmond and Weeks [26]. Our simulations will be based on these two methods, and we will provide a detailed description of each.

5.1 FARR AND GROOT ALGORITHM (1D)

Most algorithms described in the literature simulate the spherical particles in two or three dimensions. However, these algorithms often require a powerful computer to run, and depending on the number of particles used, these simulations may take several weeks to finish.

Aiming to simplify this process, Farr and Groot [63] developed an ingenious method to run the packing calculations by mapping the 3D particles into one-dimensional rods. By using this method, it is possible to estimate the random close packing fraction (ϕ_{RCP}) of each population of sphere-like particles, such as particles of carbonyl iron powder (CIP). To do so, the authors define a "distribution of diameters" (rod distribution) via the following algorithm:

Suppose that we have a random arrangement of spherical particles in a system. Now imagine that we draw a random line of size R throughout these particles, such that the portion of this random line contained within each particle creates a rod of size L_i. This is illustrated in Figure 6:
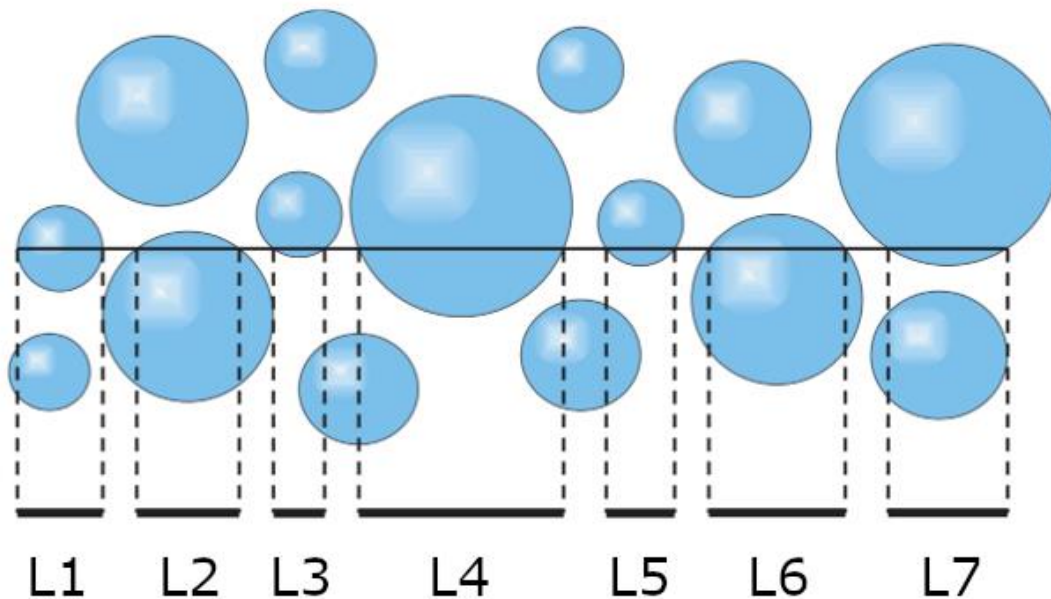
Figure 6 – By drawing a random line through an arrangement of particles, we can create a series of rods $L_1, L_2, L_3, \dots L_N$, each with probability $p(L_i)$. Source: Farr and Groot, 2009 (modified).

The probability of this random line to produce a rod of length L is given by [63]:

$$p_{1D}(L) = 2L \frac{\int_L^\infty p_{3D}(D)\,dD}{\int_0^\infty p_{3D}(D)D^2\,dD} \quad , \tag{22}$$

where $p_{3D}(D)$ is the regular particle size distribution and $p_{1D}(L)$ is the normalized, number-weighted "rod distribution" - a probability density function that expresses the frequency of each rod size. All packing calculations depend on this function.

There are several ways to implement this function computationally. The original algorithm from Farr and Groot used the inverse transform method by calculating the cumulative distribution of p_{1D}:

$$F(L) = \int_0^L p_{1D}(L')dL' \quad . \tag{23}$$

Then, a numerical method is used to compute the inverse of $F(L)$ via binary search. After the set of rods $L_1, L_2, L_3, \dots L_N$ is generated, the maximum packing fraction ψ can be estimated as:

$$\psi = \frac{\sum L_i}{R} \quad , \tag{24}$$

where R is the length of the random line. This method is extremely versatile and is also way faster than most packing algorithms. Their original version, SpherePack1D, is available for download at https://sourceforge.net/projects/spherepack1d/.

5.1.1 RCPython

Despite its usefulness, the original Farr and Groot algorithm has some limitations: so far, it only runs simulations based on Dirac delta functions and log-normal distributions. Since our goal is to study power law and Weibull models, we decided to use the theory described in Farr and Groot [63] and Farr [64] to translate their original algorithm to Python and add other types of particle size distributions.

Our modified version of the algorithm, called RCPython, will be made available online under the GNU General Public License. The full list of implemented distributions (and all their calculations) is given in Appendix B. It is worth mentioning that the algorithm of the Dirac delta function and log-normal distributions (as well as their mixtures) follow the exact same formulas used in Farr and Groot's original algorithm but translated into a different programming language.

5.1.2 Testing RCPython and Comparing Both Algorithms

To check if the RCPython algorithm is working as intended, some experimental data from Manuel *et al.* [48] were tested in both algorithms and their results were then compared.

We begin our tests by using the '-l' parameter in SpherePack1D, which computes the random close packing fraction ϕ_{RCP} based on two important constants, the $D_{4,3}$ and $D_{3,2}$. The $D_{4,3}$, also called the De Brouckere mean diameter, measures the volume-weighted mean particle size. The $D_{3,2}$, the so-called Sauter mean diameter, measures the surface-weighted mean particle size. Their definitions are given as follows [20, 64]:

$$D_{4,3} = \frac{\langle D^4 \rangle}{\langle D^3 \rangle} \quad , \tag{25}$$

$$D_{3,2} = \frac{\langle D^3 \rangle}{\langle D^2 \rangle} \quad , \tag{26}$$

where $\langle D^n \rangle = \int_0^\infty D^n P(D) dD$ is the n-th raw moment of the distribution.

The code was then entered as follows:

```
spherepack1d -l -p 3

D₄,₃ (fine)    D₃,₂ (fine)    Mass_used_in_the_mixture (fine)

D₄,₃ (medium)  D₃,₂ (medium)  Mass_used_in_the_mixture (medium)

D₄,₃ (coarse)  D₃,₂ (coarse)  Mass_used_in_the_mixture (coarse)
```

From our previous work, detailed in Manuel *et al*. [48], we know that:

Table 3 – Experimental data from each powder (volume-based)

Powder ID	D_{10} (µm)	D_{50} (µm)	D_{90} (µm)	$D_{4,3}$ (µm)	$D_{3,2}$ (µm)
#1 (Fine)	1.49	2.98	11.30	4.69	2.73
#2 (Medium)	4.57	8.29	14.46	8.99	7.44
#3 (Coarse)	6.52	18.94	42.82	23.36	13.42

Table 4 – Experimental data for each powder (number-based)

Powder ID	D_{10} (µm)	D_{50} (µm)	D_{90} (µm)	$D_{4,3}$ (µm)	$D_{3,2}$ (µm)
#1 (Fine)	0.95	1.43	2.49	4.69	2.73
#2 (Medium)	2.96	4.59	8.07	8.99	7.44
#3 (Coarse)	2.12	3.42	8.15	23.36	13.42

Also, from Manuel *et al*. [48], the following amounts of carbonyl iron powders were used to prepare the blends:

Table 5 – Amounts of powder used in the blends

Blend ID	Powder 1 (Fine) (g)	Powder 2 (Medium) (g)	Powder 3 (Coarse) (g)	Total (g)
A	0	150	0	150
B	25	100	25	150
C	50	50	50	150

Substituting the values above in SpherePack1D and RCPython, we get:

Table 6 – Maximum packing fractions of the experimental blends ($D_{4,3}$ and $D_{3,2}$)

Spherepack1D		RCPython	
Blends	ϕ_{max}	**Blends**	ϕ_{max}
A	0.694950	A	0.694950
B	0.747812	B	0.747814
C	0.792017	C	0.792019

As one can see, the results are almost identical up to five decimal places. Then, the simulations were re-run using the '$-N$' parameter, adding more rods and increasing precision:

```
spherepack1d -l -p 3 -N 100000

D₄,₃ (fine)    D₃,₂ (fine)    Mass_used_in_the_mixture (fine)

D₄,₃ (medium)  D₃,₂ (medium)  Mass_used_in_the_mixture (medium)

D₄,₃ (coarse)  D₃,₂ (coarse)  Mass_used_in_the_mixture (coarse)
```

Inputting the values from Tables 3, 4 and 5 into both algorithms, we get:

Table 7 – Maximum packing fractions of the experimental blends ($D_{4,3}$ and $D_{3,2}$, 100000 rods)

Spherepack1D		RCPython	
Blends	ϕ_{max}	**Blends**	ϕ_{max}
A	0.694953	A	0.694953
B	0.747832	B	0.747834
C	0.792039	C	0.792041

And once again, the results are practically identical. We then repeated all these simulations using another parameter: the occluded volume. According to Farr [64], the occluded volume is the total volume occupied by the particles when submerged in a liquid they are insoluble; that is, it is the volume the particles displace in an Archimedean sense. For each population of particles, their occluded volume can be computed as:

$$v_i = \frac{m_i}{\rho_i} \quad ,$$
(27)

where m_i is the mass of a given population of particles and ρ_i is the density of this population. Note that the occluded volume of each blend will vary according to the amounts of powder that were used in the formulation.

Since we need the true densities of each population of particles, the samples from Manuel *et al.* [48] were analyzed via helium pycnometry. These results are expressed in Tables 8, 9 and 10:

Table 8 – Densities and occluded volumes of each powder in blend A

Powder ID	m_i (g)	ρ_i (g.cm^{-3})	v_i (cm^3)
#1 (Fine)	0	7.7448	0
#2 (Medium)	150	7.8406	19.1312
#3 (Coarse)	0	7.8729	0

Table 9 – Densities and occluded volumes of each powder in blend B

Powder ID	m_i (g)	ρ_i (g.cm^{-3})	v_i (cm^3)
#1 (Fine)	25	7.7448	3.2280
#2 (Medium)	100	7.8406	12.7541
#3 (Coarse)	25	7.8729	3.1754

Table 10 – Densities and occluded volumes of each powder in blend C

Powder ID	m_i (g)	ρ_i (g.cm^{-3})	v_i (cm^3)
#1 (Fine)	50	7.7448	6.4559
#2 (Medium)	50	7.8406	6.3771
#3 (Coarse)	50	7.8729	6.3509

The following code was then entered in SpherePack1d:

```
spherepack1d -l -p 3

D4,3 (fine)    D3,2 (fine)    Occluded_Volume_of_the_Powder (fine)

D4,3 (medium) D3,2 (medium) Occluded_Volume_of_the_Powder (medium)

D4,3 (coarse) D3,2 (coarse) Occluded_Volume_of_the_Powder (coarse)
```

The values from Tables 8, 9 and 10 were inputted in both algorithms, generating:

Table 11 – Maximum packing fractions of the experimental blends (Occluded volume)

Spherepack1D		RCPython	
Blends	ϕ_{max}	**Blends**	ϕ_{max}
A	0.694950	A	0.694950
B	0.748128	B	0.748130
C	0.792099	C	0.792101

We can see that the results are extremely close. Finally, the simulations were repeated in both algorithms one last time with an increased number of rods:

```
spherepack1d -l -p 3 -N 100000

D4,3 (fine)    D3,2 (fine)    Occluded_Volume_of_the_Powder (fine)

D4,3 (medium) D3,2 (medium) Occluded_Volume_of_the_Powder (medium)

D4,3 (coarse) D3,2 (coarse) Occluded_Volume_of_the_Powder (coarse)
```

Then we got:

Table 12 – Maximum packing fractions of the experimental blends (Occluded volume, 100000 rods)

Spherepack1D		RCPython	
Blends	ϕ_{max}	**Blends**	ϕ_{max}
A	0.694953	A	0.694953
B	0.748148	B	0.748150
C	0.792121	C	0.792123

We can see once more that the results were practically the same. Therefore, it is safe to conclude that RCPython correctly reproduces the results from SpherePack1D.

5.1.3 Implementing new probability distributions

After translating the algorithm, it is straightforward to add new distributions to it. The steps below can be used to add any type of distribution to the code and were taken directly from Farr [64]:

1. Start the computations by calculating the number-weighted rod distribution (p_{1D}) using equation 22:

$$p_{1D}(L) = 2L \frac{\int_L^\infty p_{3D}(D)dD}{\int_0^\infty p_{3D}(D)D^2\, dD} \quad,$$

   where D is the diameter, $p_{3D}(D)$ is a number-weighted probability distribution, and L is the rod length.

2. Then, we compute the cumulative distribution of p_{1D} using equation 23:

$$F(L) = \int_0^L p_{1D}(L')dL' \quad.$$

   Now, compute the inverse of the cumulative distribution, that is, $F^{-1}(L)$. This function will sample the rod sizes.

   Remark: This process can be done analytically or numerically. The method used in Farr [64] is numerical and uses a type of algorithm called binary search [65].

3. Finally, generate a list of lengths such that:

$$L_i = F^{-1}\left(\frac{2N-2i+1}{2N}\right) \quad. \tag{28}$$

Lists are easily created in Python and can be passed as arguments to equations 22, 23 and 28 to compute the rod sizes. To better illustrate this procedure, we will compute these equations for the Dirac delta function.

The Dirac delta function describes a monodisperse arrangement of spheres and is defined as [66]:

$$\delta(x - x_0) = \begin{cases} \infty, & if \ x = x \ , \\ 0, & if \ x \neq x_0 \ . \end{cases} \tag{29}$$

And, therefore, a probability distribution of monodisperse spheres is given by:

$$p_{3D}(D) = \delta(D - D_0) \ , \quad -\infty < D < \infty \ , \tag{30}$$

where D_0 is the mean size of the particles. From equation 22 we know that a rod distribution is computed as:

$$p_{1D}(L) = 2L \frac{\int_L^\infty p_{3D}(D) \, dD}{\int_0^\infty p_{3D}(D) D^2 \, dD} \ .$$

Substituting the function $p_{3D}(D)$ with the Dirac delta function, we get:

$$p_{1D}(L) = 2L \frac{\int_L^\infty \delta(D - D_0) \, dD}{\int_0^\infty \delta(D - D_0) D^2 \, dD} \ .$$

The integral from the denominator can be reduced to:

$$p_{1D}(L) = 2L \frac{\int_L^\infty \delta(D - D_0) \, dD}{D_0^2} \ .$$

But one must be extra careful with the integral on the numerator, since it goes from $[L, \infty)$, instead of $(-\infty, \infty)$.

To solve this integral, we must remember that there is a well-defined relationship between the Dirac Delta function and the Heaviside step function θ [66]:

$$\int_{-\infty}^{D} \delta(D' - D_0)dD' = \theta(D - D_0) .$$ (31)

By taking the original integral from the delta function and splitting it in two parts, we get:

$$\int_{-\infty}^{\infty} \delta(D - D_0)dD = \int_{-\infty}^{L} \delta(D - D_0)dD + \int_{L}^{\infty} \delta(D - D_0)dD .$$

And:

$$1 = \theta(L - D_0) + \int_{L}^{\infty} \delta(D - D_0)dD .$$

Therefore:

$$\int_{L}^{\infty} \delta(D - D_0)dD = 1 - \theta(L - D_0) .$$

The Heaviside step function has an important identity:

$$\theta(x - x_0) + \theta(x_0 - x) = 1 .$$

Therefore:

$$\int_{L}^{\infty} \delta(D - D_0)dD = \theta(D_0 - L) .$$

And we finally get:

$$p_{1D}(L) = \frac{2L}{D_0^2} \theta(D_0 - L) = \begin{cases} \dfrac{2L}{D_0^2}, & if\ L \leq D_0 , \\ 0, & if\ L > D_0 . \end{cases}$$

Now, we calculate the cumulative rod distribution:

$$F(L) = \int_0^L p_{1D}(L')dL' \; .$$

Since the function above is defined piecewise, we have:

$$F(L) = \begin{cases} \int_0^L \dfrac{2L'}{D_0^2}dL', & if \; L \leq D_0 \; , \\ 0, & if \; L > D_0 \; . \end{cases}$$

And therefore:

$$F(L) = \begin{cases} \left(\dfrac{L}{D_0}\right)^2, & if \; L \leq D_0 \; , \\ 0, & if \; L > D_0 \; . \end{cases}$$

The inverse of $F(L)$ was then implemented numerically in Python via binary search.

5.1.4 Reading histograms

One useful feature added to RCPython is the ability to compute the maximum packing fraction based on number-sized histograms, that is, raw experimental data. This feature was developed in collaboration with Dr. Eric R. Weeks and Emory University and closely follow the methods described in section 4.3 of Farr [64]. The calculations are made as described below.

We start by assuming that we have a mixture of two particle sizes D_1 and D_2, with $D_2 > D_1$ and such that:

$$p_{3D}(D) = \frac{1}{2}\delta(D - D_1) + \frac{1}{2}\delta(D - D_2) \; .$$

Then, using the Farr and Groot algorithm, we would have:

$$p_{1D}(L) = 2L \frac{\int_L^\infty \left[\delta \frac{1}{2}\delta(D-D_1)+\frac{1}{2}\delta(D-D_2)\right]dD}{\int_0^\infty \left[\delta\frac{1}{2}\delta(D-D_1)+\frac{1}{2}\delta(D-D_2)\right]D^2\,dD} \ .$$

The integral from the denominator quickly evaluates to:

$$p_{1D}(L) = 2L \frac{\int_L^\infty \left[\delta\frac{1}{2}\delta(D-D_1)+\frac{1}{2}\delta(D-D_2)\right]dD}{\frac{1}{2}\left[D_1^2+D_2^2\right]} \ .$$

The integral on the numerator, however, must be treated carefully, since it goes from $[L,\infty)$, instead of $(-\infty,\infty)$. As with the Dirac Delta functions, we need to make sure that it includes all the "peaks". Therefore, we must split the integral into three parts:

$$\int_L^\infty \left[\delta\frac{1}{2}\delta(D-D_1)+\frac{1}{2}\delta(D-D_2)\right]dD = \begin{cases} 1, & if\ L < D_1 \ , \\ \frac{1}{2}, & if\ D_1 < L < D_2 \ , \\ 0, & if\ L > D_2 \ . \end{cases}$$

And the rod distribution for a mixture of two monodisperse population quickly becomes:

$$p_{1D}(L) = \begin{cases} 4L/(D_1^2 + D_2^2), & if\ L < D_1 \ , \\ 2L/(D_1^2 + D_2^2), & if\ D_1 < L < D_2 \ , \\ 0, & if\ L > D_2 \ . \end{cases} \tag{32}$$

This argument can be generalized to a sum of N monodisperse distributions $D_1, D_2, D_3, \dots, D_N$. To do so, suppose that we have a mixture of N particle populations such that:

$$p_{3D}(D) = \frac{1}{N}\delta(D-D_1) + \frac{1}{N}\delta(D-D_2) + \frac{1}{N}\delta(D-D_3) + \cdots + \frac{1}{N}\delta(D-D_N) \ .$$

Then, via the Farr and Groot algorithm, we get:

$$p_{1D}(L) = 2L \frac{\int_L^\infty \left[\frac{1}{N}\delta(D-D_1)+\frac{1}{N}\delta(D-D_2)+\frac{1}{N}\delta(D-D_3)+\cdots+\frac{1}{N}\delta(D-D_N)\right]dD}{\int_0^\infty \left[\frac{1}{N}\delta(D-D_1)+\frac{1}{N}\delta(D-D_2)+\frac{1}{N}\delta(D-D_3)+\cdots+\frac{1}{N}\delta(D-D_N)\right]D^2\,dD} \quad.$$

The integral from the denominator quickly evaluates to:

$$p_{1D}(L) = 2L \frac{\int_L^\infty \left[\frac{1}{N}\delta(D-D_1)+\frac{1}{N}\delta(D-D_2)+\frac{1}{N}\delta(D-D_3)+\cdots+\frac{1}{N}\delta(D-D_N)\right]dD}{\frac{1}{N}\left[D_1^2+D_2^2+D_3^2+\cdots+D_N^2\right]} \quad.$$

But the integral on the numerator, again, must be treated carefully, and we need to make sure that it includes all the "peaks". To do so, we split the integral into $N+1$ parts:

$$\int_L^\infty p_{3D}(D)dD = \begin{cases} 1, & if\ L < D_1 \quad, \\ (N-1)/N, & if\ D_1 < L < D_2 \quad, \\ (N-2)/N, & if\ D_2 < L < D_3 \quad, \\ (N-3)/N, & if\ D_3 < L < D_4 \quad, \\ \qquad\vdots \\ 1/N, & if\ D_{N-1} < L < D_N \quad, \\ 0, & if\ L > D_N \quad. \end{cases}$$

And the rod distribution for a mixture of N monodisperse population becomes:

$$p_{1D}(L) = \begin{cases} 2NL/(D_1^2+D_2^2+D_3^2+\cdots+D_N^2), & if\ L < D_1 \quad, \\ 2(N-1)L/(D_1^2+D_2^2+D_3^2+\cdots+D_N^2), & if\ D_1 < L < D_2 \quad, \\ 2(N-2)L/(D_1^2+D_2^2+D_3^2+\cdots+D_N^2), & if\ D_2 < L < D_3 \quad, \\ 2(N-3)L/(D_1^2+D_2^2+D_3^2+\cdots+D_N^2), & if\ D_3 < L < D_4 \quad, \\ \qquad\vdots \\ 2(1)L/(D_1^2+D_2^2+D_3^2+\cdots+D_N^2), & if\ D_{N-1} < L < D_N \quad, \\ 0, & if\ L > D_N\ . \end{cases} \qquad (33)$$

Then, via the inversion method, we can calculate the CDF of this distribution:

$$F(L) = \int_0^L p_{1D}(L')dL' \quad.$$

For two populations of particles, we get:

$$F(L) = \begin{cases} 2L'^2/(D_1^2 + D_2^2), & if\ L < D_1\ , \\ (D_1^2 + L'^2)/(D_1^2 + D_2^2), & if\ D_1 < L < D_2\ , \\ 1,\ if\ L > D_2\ . \end{cases} \tag{34}$$

And for N populations of particles, we finally get:

$$F(L) = \begin{cases} NL'^2/(D_1^2 + D_2^2 + D_3^2 + \cdots + D_N^2)\ ,\ if\ L' < D_1\ , \\ [D_1^2 + (N-1)L'^2]/(D_1^2 + D_2^2 + D_3^2 + \cdots + D_N^2),\ if\ D_1 < L' < D_2\ , \\ [D_1^2 + D_2^2 + (N-2)L'^2]/(D_1^2 + D_2^2 + D_3^2 + \cdots + D_N^2),\ if\ D_2 < L' < D_3\ , \\ [D_1^2 + D_2^2 + D_3^2 + (N-3)L'^2]/(D_1^2 + D_2^2 + D_3^2 + \cdots + D_N^2),\ \ if\ D_3 < L' < D_4\ , \\ \quad\quad\quad\quad\quad\quad\vdots \\ [D_1^2 + D_2^2 + D_3^2 + \cdots + D_{N-1}^2 + L'^2]/(D_1^2 + D_2^2 + D_3^2 + \cdots + D_N^2),\ if\ D_{N-1} < L' < D_N\ , \\ 1,\ if\ L' > D_N\ . \end{cases} \tag{35}$$

The inverse function of the integral $F(L)$ can then be computed numerically (via binary search) or analytically to generate values following $p_{1D}(L)$.

5.2 DESMOND AND WEEKS ALGORITHM (3D)

We have already defined a one-dimensional algorithm that approximates the maximum packing fraction using one-dimensional rods. Now, we will establish a more accurate, three-dimensional version of these calculations. To do so, we will follow the same methodology from a previous work, which is detailed in Manuel *et al*. [48]. Also, note that we will be using the radius R instead of the diameter D in all the calculations of this method.

Then, in order to compute the random close packing volume fractions of our size distributions, we will follow the computational methods from Xu, Blawzdziewicz, and O'Hern [47], and Desmond and Weeks [26, 67]. We begin by taking the experimentally determined particle size distribution and generating N random particle radii consistent with the desired particle size distribution. Then, we randomly place these N particles in a large cubical box with periodic boundary conditions, with the box size chosen so that the starting volume fraction is 1% (or 0.1% if the ratio of largest particle radius to smallest is larger than 50).

Starting from this initial condition, we gradually increase the size of all particles in small steps and move the particles that overlap until we reach a close packed state. Specifically, at each size increase step, we expand the particles by multiplying their radii by 1 + ε, so that the particle size distribution remains unchanged except for the overall scale. In particular, the polydispersity, skewness, and kurtosis remain unchanged. After an expansion step, we then examine all particles that are touching another particle. We treat each particle as a soft particle with an interaction potential that is equal to the square of the overlap of each particle pair. That is, this potential goes smoothly to zero at the separation distance r_{ij} equal to the sum of the two particle radii ($R_i + R_j$); and the potential increases as $(R_i + R_j - r_{ij})^2$ when particles overlap. We consider overlapping particles in random order, moving an individual particle via two conjugate gradient steps to minimize the interaction energy, hopefully to zero. For any particles not in contact with any other particles, we move them a small random step (if that does not cause any new overlaps). This random step facilitates finding dense packings. When the total system energy is reduced below a numerical tolerance, the next expansion step is tried.

At some point, the total system energy cannot be reduced below the chosen tolerance. The program then reverts to a lower volume fraction, reduces the expansion factor ε, and then tries another expansion step. This is repeated until no expansion seems to be possible. At this point, the computation slightly decreases the size of all particles (by a uniform multiplicative factor) so that the energy is strictly zero, which is to say that no particles are overlapping at all, and this determines the final random close packing state for the N particles.

We then repeat this process many times for N = 300, 400, 800, and 1600 particles; each repetition is performed with a new set of N random particle sizes drawn from a desired particle size distribution. For each N, we then compute the mean random close packing volume fraction. Following the work of Desmond and Weeks [67], we note that the mean volume fraction grows linearly with $N^{-1/3}$, thus allowing us to extrapolate to the N → ∞ limit and then compute the maximum packing fraction. For a perfectly monodisperse packing, this algorithm yields ϕ_{RCP} = 63.6 ± 0.1%, in good agreement with experimental observations.

5.3 RUNNING THE PARTICLE SIMULATIONS

Finally, the algorithms described in sections 5.1 and 5.2 were used to compute the maximum packing fractions of our spheroidal carbonyl iron powders. These calculations were performed for the volume-weighted power laws and the number-weighted Weibull distribution. The goal was to test how well the power laws and Weibull distributions estimate the packing efficiency and to search for an optimum configuration that creates the highest maximum packing fraction, and consequently, the lowest possible viscosity. These results are detailed in the following sections.

6 RESULTS AND DISCUSSION

After defining our methodology, it is now possible to run the simulations and check how well our algorithms can estimate the packing fractions of the power law and Weibull models.

6.1 SIMULATION RESULTS – DINGER-FUNK DISTRIBUTION

We shall start with the Dinger-Funk distribution since it is the modern version of the Andreasen-Andersen model and also because, due to the truncation, it always converges. According to the theory proposed by Dinger and Funk, in order to obtain the densest possible arrangement, the distribution modulus must be $q = 0.37$ in 3D systems. Therefore, by plotting the maximum packing fraction against the distribution modulus, we should expect an optimum point around this region.

For a fixed number of rods ($N = 16000$, which is the default value used by SpherePack1D), the following exponents from the Dinger-Funk distribution were tested in RCPython:

Table 13 – Maximum packing fractions of the Dinger-Funk distribution (RCPython, 16000 rods, number-weighted, $D_{min} = 0.1\,\mu m$, $D_{max} = 50\,\mu m$)

Distribution Modulus (q)	ϕ_{max}
-1	0.689700
-0.50	0.750065
0	0.847714
0.30	0.903343
0.35	0.910615
0.37	0.913323
0.40	0.917162
0.45	0.922954
0.50	0.923939
0.55	0.918213
0.60	0.909825
1	0.831217
1.5	0.755432
2	0.719430
2.5	0.698070
3	0.684398
3.5	0.675150
4	0.668625

These data allow us to plot the following graph:

Figure 7 - The optimum packing fraction of the volume-weighted Dinger-Funk
distribution with size range 0.1 – 50 µm. Source: Author, 2024

Note that the optimum point is located at $q = 0.5$, which is not far from the value predicted by Dinger and Funk ($q = 0.37$). What is even more interesting, however, is that this trend also appears for wider size ranges: for a distribution with $D_{min} = 0.1\ \mu m$ and $D_{max} = 100\ \mu m$, we have:

Table 14 – Maximum packing fractions of the Dinger-Funk distribution
(RCPython, 16000 rods, number-weighted, $D_{min} = 0.1\ \mu m$, $D_{max} = 100\ \mu m$)

Distribution Modulus (q)	ϕ_{max}
-1	0.689862
-0.50	0.752923
0	0.861280
0.30	0.922010
0.35	0.929588
0.37	0.932378
0.40	0.936305
0.45	0.941984
0.50	0.939432
0.55	0.931093
0.60	0.922553
1	0.840337
1.5	0.755680
2	0.719436
2.5	0.698070
3	0.684398
3.5	0.675150
4	0.668625

This allows us to plot the following graph:
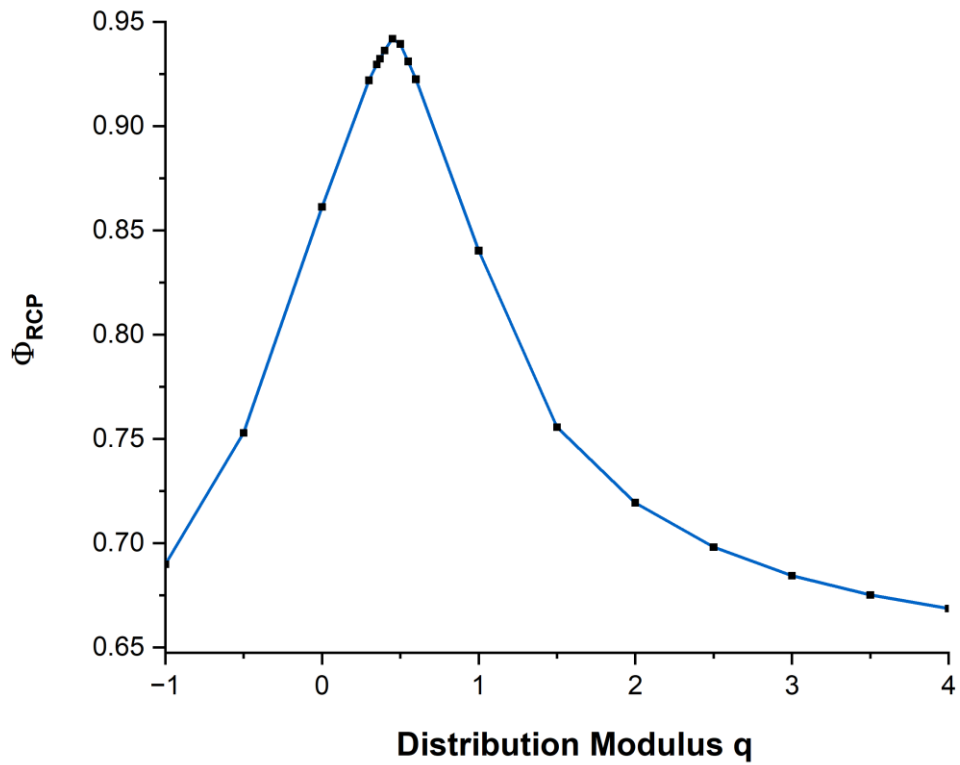
Figure 8 - The optimum packing fraction of the volume-weighted Dinger-Funk distribution with size range 0.1 – 100 μm. Source: Author, 2024

For a distribution with $D_{min} = 0.1\ \mu m$ and $D_{max} = 1000\ \mu m$, we have:

Table 15 – Maximum packing fractions of the Dinger-Funk distribution

(RCPython, 16000 rods, number-weighted, $D_{min} = 0.1\ \mu m$, $D_{max} = 1000\ \mu m$)

Distribution Modulus (q)	ϕ_{max}
-1	0.689923
-0.50	0.756266
0	0.893029
0.30	0.961735
0.35	0.968519
0.37	0.970887
0.40	0.974096
0.45	0.975789
0.50	0.972384
0.55	0.971825
0.60	0.970894
1	0.881235
1.5	0.756390
2	0.719438
2.5	0.698070
3	0.684398
3.5	0.675150
4	0.668625

This allows us to plot the following graph:

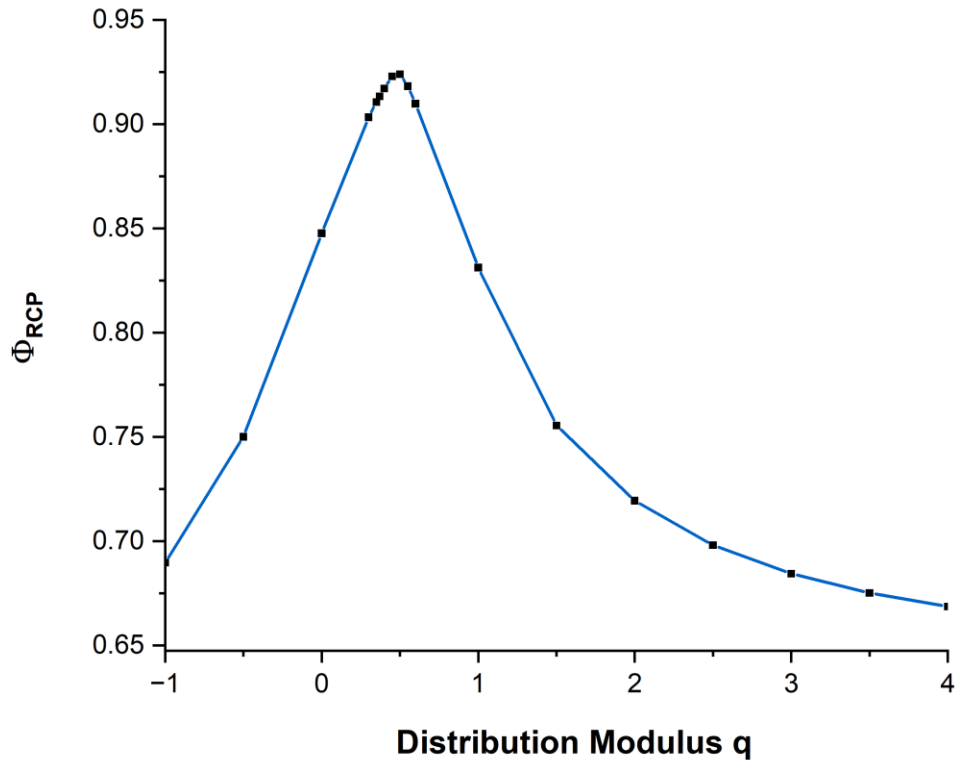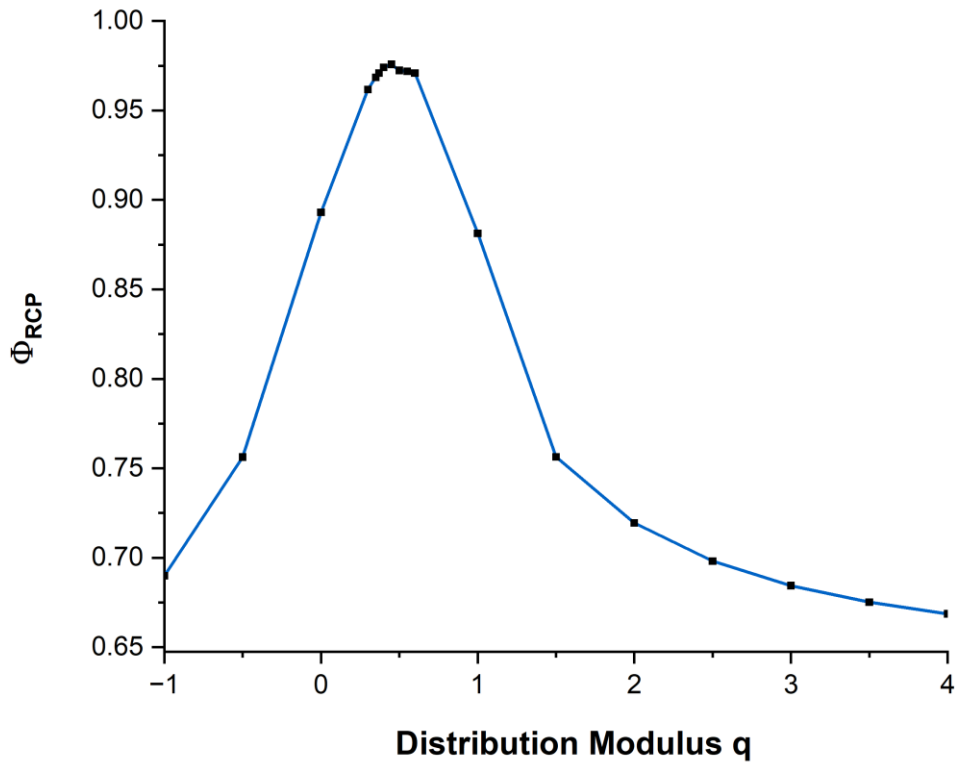**Figure 9** - The optimum packing fraction of the volume-weighted Dinger-Funk
distribution with size range 0.1 – 1000 µm. Source: Author, 2024

Therefore, this "peak" seems to appear independently of the size range of our particles. We can also plot the three graphs together, to analyze the dependency of the maximum packing fraction on the size ratio of our particles. This is depicted in Figure 10:
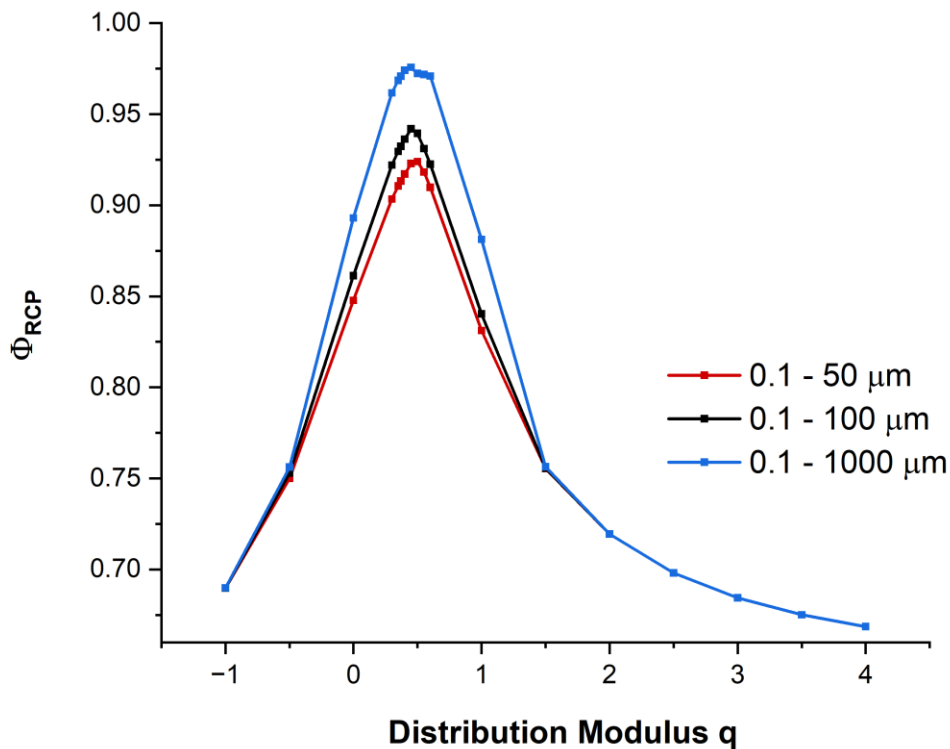
Figure 10 - The optimum packing fraction depends on the size range.
Source: Author, 2024.

As we can see, the greater the ratio D_{max}/D_{min}, the greater the packing. But we can extend our tests even further: to ensure the accuracy and consistency of our results, we can run more simulations with the same exponents, but this time using the 3D algorithm. This should allow us to rigorously validate our data and check how well the results agree by using a different type of simulation.

Assuming a size ratio $D_{max}/D_{min} = 100$, the following exponents were tested:

Table 16 – Maximum packing fractions of the Dinger-Funk model

(3D algorithm, volume-weighted, size ratio = 100)

Distribution Modulus (q)	ϕ_{max}
-1	0.691998
-0.5	0.721206
0.1	0.779553
0.30	0.802665
0.40	0.811636
0.5	0.802592
0.6	0.796253
0.8	0.761905
2	0.697348
3	0.6720086
4	0.657323

Based on these data, we can plot the following graph:
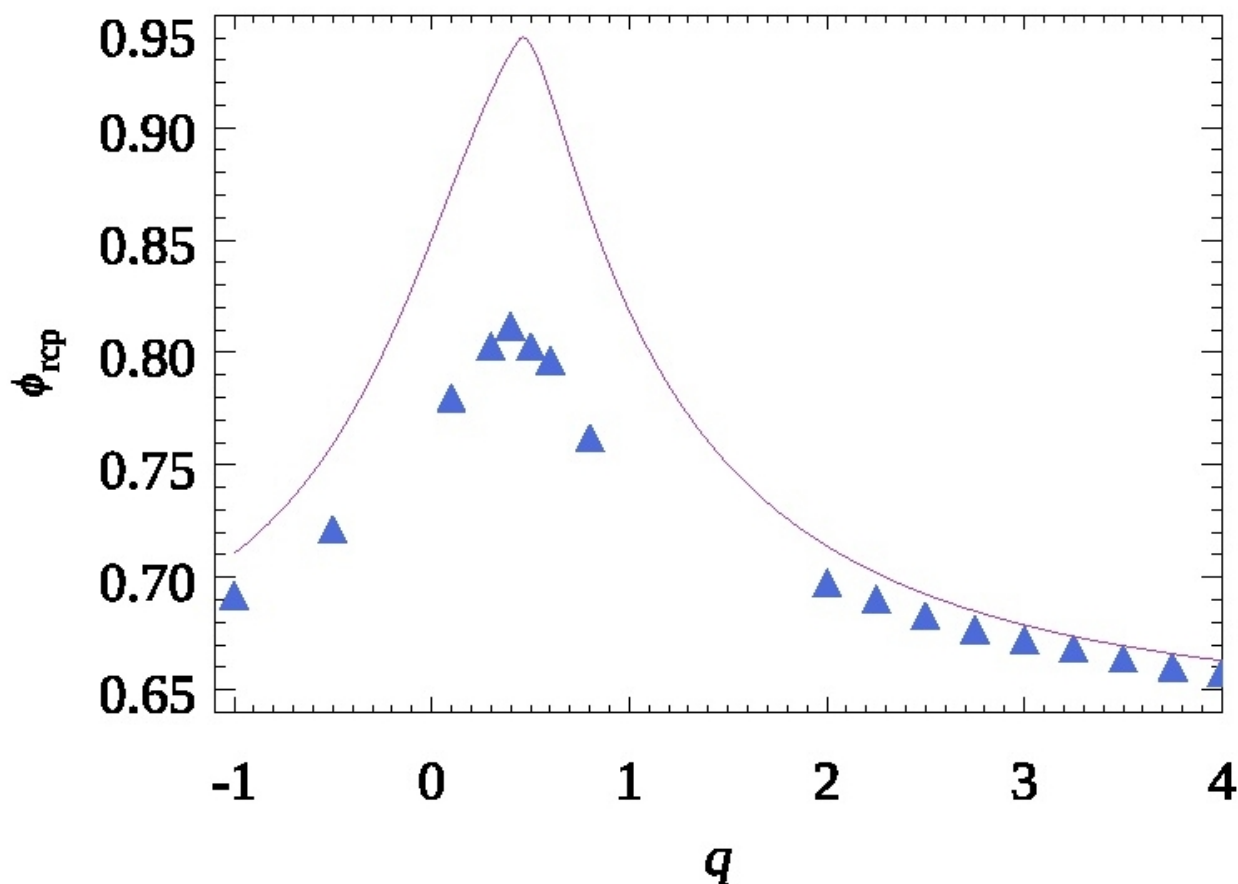
Figure 11 – The optimum packing fraction generated by a Dinger-Funk distribution. Both simulations, 1D (purple line) and 3D (blue triangles), predicted an optimum packing fraction at around 0.40. Source: Author, 2024.

Although the packings generated by the 1D (purple line) and 3D (blue triangles) simulations are slightly different, both algorithms predicted an optimum packing fraction at around $q \approx 0.40$. This value is not only close to what Dinger and Funk predicted ($q \approx 0.37$), but also agrees well with results already published in the recent literature [68, 69]. However, one must take care with the overestimation generated by the 1D algorithm since packings of 95% would be hard to achieve experimentally. Also, we can expect the 3D algorithm to be more accurate since it runs several simulations with different numbers of particles and then computes the mean random close packing fraction via extrapolation.

6.2 SIMULATION RESULTS – ANDREASEN-ANDERSEN

We can also use the previous methods to test the Andreasen-Andersen distribution. According to their model, the maximum packing fraction of a population of particles can be estimated through a "regular" power law. Also, if the distribution modulus falls anywhere between $1/3 < q < 1/2$, this packing is optimum and generates the lowest possible viscosity. With that in mind, we can plot the following graph:
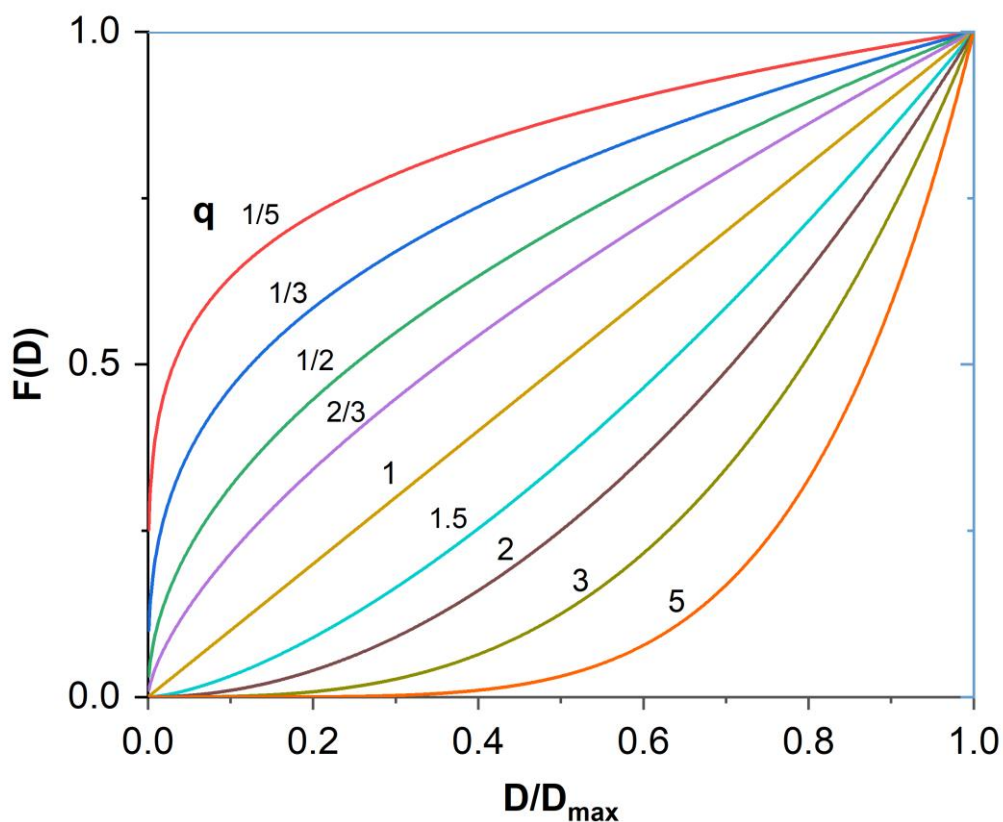
Figure 12 – The Andreasen-Andersen model for several q exponents. Source: Author, 2024.

By analyzing Figure 12, we can notice that the region between $1/3 < q < 1/2$ is located between the blue and green lines. Any packing outside this region will be non-optimum and will generate higher viscosities for our magnetorheological fluids. With that in mind, we shall test several exponents inside and outside this region and check their packing fractions.

For the same fixed number of rods ($N = 16000$, which is the default value used by SpherePack1D), and by assuming that $D_{max} = 100\ \mu m$, the following exponents were tested:

Table 17 – Maximum packing fractions of the Andreasen-Andersen equation for different exponents (RCPython, 16000 rods, $D_{max} = 100\ \mu m$, volume-weighted)

Distribution Modulus (q)	ϕ_{max}
0.01	1.000000
0.05	0.996720
0.1	0.945767
0.15	0.876791
0.2	0.835152
0.3	0.796649
0.4	0.771821
0.5	0.756857
0.75	0.734940
1	0.719438
1.5	0.698070
2	0.684398
2.5	0.675150
3	0.668625
4	0.660293
5	0.655407
10	0.647002
100	0.643520

We can plot the following graph:
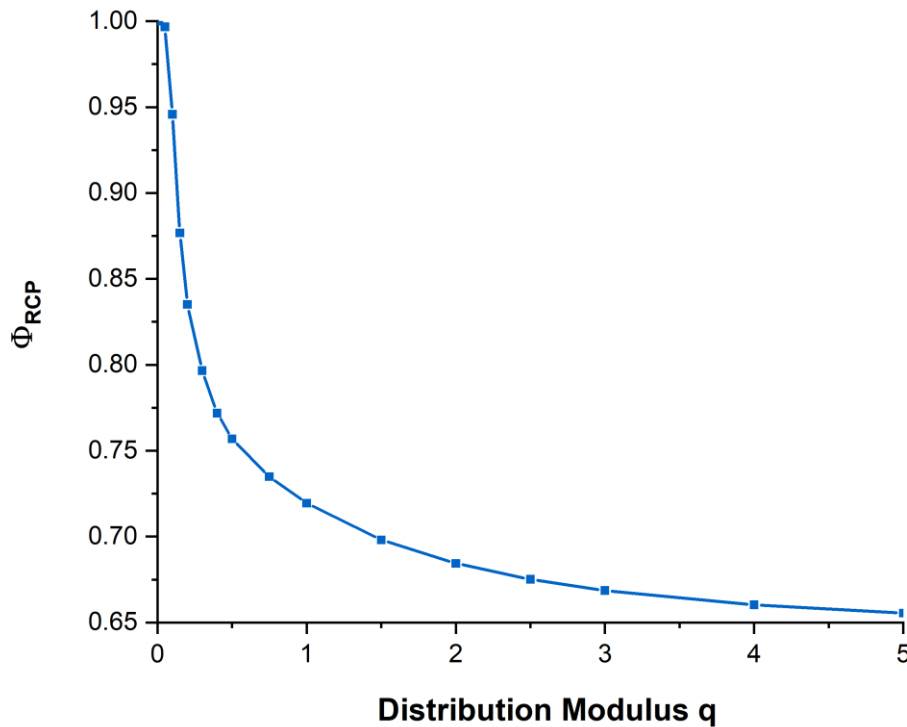
Figure 13 - The maximum packing fraction × distribution modulus results for the volume-weighted Andreasen-Andersen distribution. Source: Author, 2024.

Compare this plot to Figures 7 - 10: due to the mathematical definition of the power law, the Andreasen-Andersen distribution is not well-behaved. Since it is not doubly truncated, the packing efficiency diverges for some values of the algorithm, and it fails to describe the regions below $q < 0$. As a result, the algorithm overflows and we cannot estimate an optimum packing fraction since the behavior of the function is asymptotic.

The main power law results, however, arise from the Dinger-Funk distribution: the data show that we can optimize the off-state viscosity of an MRF by carefully adjusting the distribution modulus of a truncated power law. In fact, if these results are confirmed experimentally, they should allow us to reduce the viscosity of MRF in general and prepare fluids with even greater magnetorheological effects.

6.3 SIMULATION RESULTS – WEIBULL DISTRIBUTION

Recall from section 4 that the number-weighted Weibull distribution is an extremely flexible function due to its three parameters: location (a), scale (b), and shape (c). Therefore, to better analyze how these parameters will influence the polydispersity, we must change their values as little as possible.

We will start by analyzing the influence of the shape factor on the packing of the solid particles. As should be expected, even small changes in this parameter can cause significant changes in the overall shape of the distribution. This is illustrated in Figure 14:
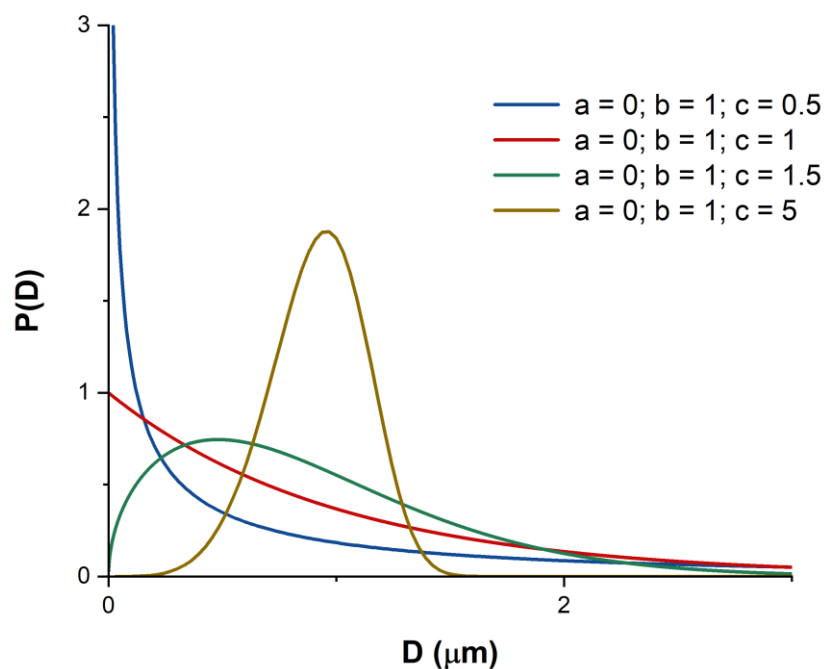
Figure 14 - By adjusting only the shape parameter c, it is possible to get many shapes of the Weibull distribution, each with different packing efficiencies. Source: Author, 2024

However, it also causes significant changes in the polydispersity of the solid particles:

Table 18 – Maximum packing fractions of the Weibull distribution for different shape parameters

(RCPython, number-weighted, 16000 rods)

Distribution	Shape Parameter (c)	Polydispersity Index (α)	ϕ_{max}
Blue	0.5	10	0.771422
Red	1.0	1	0.720659
Green	1.5	0.42	0.697482
Golden	5.0	0.05	0.656684

As we can see, there seems to be an inverse relationship between the shape parameter c and the maximum packing fraction. By increasing the shape parameter, we decrease the packing efficiency. This result makes sense if we consider the polydispersity index (coefficient of variation) of the number-weighted Weibull distribution, which is described in equation 36:

$$\alpha = \frac{\sigma}{\mu} = \frac{b^2\left[\Gamma\left(1+\frac{2}{c}\right)-\Gamma^2\left(1+\frac{1}{c}\right)\right]}{b\Gamma\left(1+\frac{1}{c}\right)+a} \quad . \tag{36}$$

From the formula above, we can see that by increasing the shape parameter, the coefficient of variation gets smaller and smaller and, therefore, the polydispersity decreases. However, it is also worth mentioning that we must avoid choosing a minimum particle size that is too small; otherwise, the MR effect is lost, and the suspension becomes a ferrofluid. Now, consider three different Weibull distributions centered around the same mode, as illustrated in Figure 15:
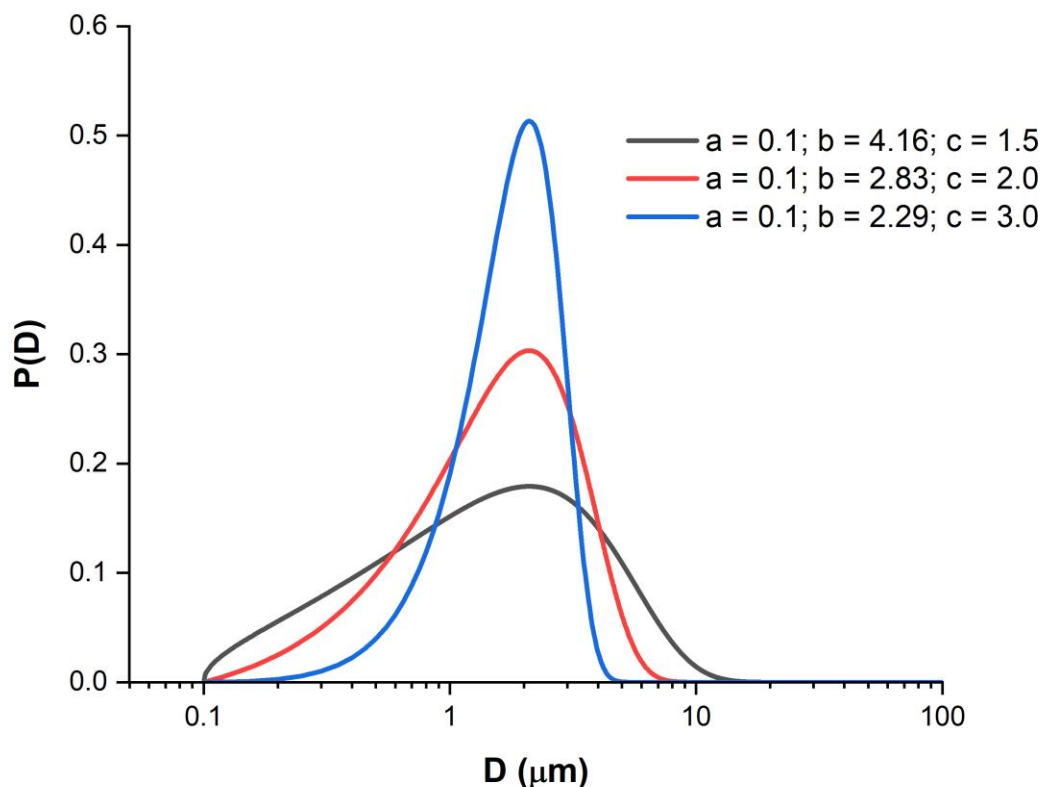
Figure 15 - By centering the distributions around the same mode, it is possible to better analyze their polydispersity. Source: Author, 2024

By inputting the parameters a, b, and c from Figure 15 into RCPython, we get the following values of ϕ_{Max}:

Table 19 – Maximum packing fractions of the Weibull distribution centered around the same mean (RCPython, number-weighted, 16000 rods)

Distribution	Polydispersity Index (α)	ϕ_{max}
Blue	0.26	0.664659
Red	0.66	0.680572
Black	1.69	0.695474

As we can see, broadening the size distribution can increase the maximum packing fraction. This result is in good agreement with what we previously reported in Manuel *et al.* [48] and shows that, independently of the size distribution, greater ranges of particle sizes can contribute even further to the polydispersity of the solid phase. Also, note that the modes in Figure 15 do not need to be matched, since the maximum packing fraction is independent of the mode.

7 CONCLUSIONS

Magnetorheological fluids are smart materials whose properties are directly influenced by the packing of their solid phase. By carefully adjusting the concentration, size, and particle size distribution of its magnetic particles, it is possible to greatly improve the magnetorheological effect, which is responsible for its most relevant properties. Depending on the particle size distribution utilized, the relative viscosity of these fluids can be significantly enhanced, and, in this context, the power law and Weibull distributions arise as well-established methods to adjust the solid phase. In this work, we have studied three statistical models, the Andreasen-Andersen distribution, the Dinger-Funk distribution, and the Weibull distribution. By modifying a powerful algorithm from the literature, we were able to study these models in-depth and explain their significance in the context of magnetorheology. According to the data, the Dinger-Funk model is well-behaved and gives an optimum packing fraction that should allow us to reduce the viscosity of future magnetorheological formulations significantly. The Andreasen-Andersen, however, is mathematically limited and did not prove useful in predicting an optimum packing fraction for the magnetic particles. The Weibull distribution proved useful not only as a good model to describe the solid phase, but also as a very flexible function that can be used to design many shapes of histograms. As a proposal for future works, we suggest investigating whether the observed behavior can be applied in practice in magnetorheology and if it works with other smart materials, such as magnetorheological gels and electrorheological fluids, in addition to MRF with different materials and volume fractions. These results, however, are not restricted to magnetorheology. Since the algorithms use geometric arguments throughout their calculations, we expect them to be useful in several other areas of science and engineering, especially when working with particulate materials.

8 ACKNOWLEDGEMENTS

9 REFERENCES

[1] De Vicente J, Klingenberg D, Hidalgo-Alvarez R. Magnetorheological fluids: a review. Soft Matter. 2011; 7:3701–10.

[2] Olabi A G, Grunwald A. Design and application of magneto-rheological fluid. Mater. Des. 2007; 28:2658–64.

[3] Tang H. Particle size polydispersity of the rheological properties in magnetorheological fluids. Sci. China Phys. Mech. Astron. 2011; 54:1258–62.

[4] López-López M, Kuzhir P, Meunier A, Bossis G. Synthesis and magnetorheology of suspensions of submicron-sized cobalt particles with tunable particle size. J. Phys.: Condens. Matter. 2010; 22:324106.

[5] Carlson J D, Jolly M R. MR fluid, foam and elastomer devices. Mechatronics; 2000; 10:555–69.

[6] Cao J, Li J, Nie M, Zhu P, Zhao C, Zhang J *et al*. A novel surface polishing method and its fundamental performance in ultra-fine polishing of wafer. Int. J. Adv. Manuf. Technol. 2019; 105:2919–33.

[7] Jiang N, Sun S, Ouyang Y, Xu M, Li W, Zhang S. A highly adaptive magnetorheological fluid robotic leg for efficient terrestrial locomotion. Smart Mater. Struct. 2016 ; 25:095019.

[8] El Wahed A, Balkhoyor L. The performance of a smart ball-and-socket actuator applied to upper limb rehabilitation. J. Intell. Mater. Syst. Struct. 2018; 29:2811–22.

[9] El Wahed A. A novel hydraulic actuation system utilizing magnetorheological fluids for single-port laparoscopic surgery applications. Materials. 2020; 13:1380.

[10] Park B J, Fang F F, Choi H. Magnetorheology: materials and application. Soft Matter. 2010; 6:5246.

[11] Anupama A, Kumaran V, Sahoo B. Effect of magnetic dipolar interactions and size dispersity on the origin of steady state magnetomechanical response in bidisperse Mn–Zn ferrite spherical particle based magnetorheological fluids. New J. Chem. 2019; 43:9969–79.

[12] Gomes de Sousa S R, Bombard A J F. Redispersibility and its relevance in the formulation of magnetorheological fluids. In: Seung-Bok C, Weihua L, editors. Magnetorheological Materials and Their Applications. London: IET—The Institution of Engineering and Technology; 2019. p 1–18.

[13] Guerrero-Sanchez C, Lara-Ceniceros T, Jimenez-Regalado E, Ras¸a M, Schubert U. Magnetorheological fluids based on ionic liquids. Adv. Mater. 2007; 19:1740–7.

[14] Shah K, Choi S. The field-dependent rheological properties of magnetorheological fluids featuring plate-like iron particles. Front. Mater. 2014; 1:1–6.

[15] Farris R. Prediction of the viscosity of multimodal suspensions from unimodal viscosity data. Trans. Soc. Rheol. 1968; 12:281–301.

[16] Foister R. Magnetorheological fluids. 1997; United States Patent 5,667,715.

[17] Morillas J, de Vicente J. Magnetorheology: a review. Soft Matter. 2020; 16:9614–9642.

[18] Pednekar S, Chun J, Morris J. Bidisperse and polydisperse suspension rheology at large solid fraction. J. Roehl. 2018; 62:513–26.

[19] Ota M, Miyamoto T. Optimum particle size distribution of an electrorheological fluid. J. Appl. Phys. 1994; 76:5528–32.

[20] Allen T. Particle Size Measurement: Powder sampling and particle size measurement. 5. ed. London: Chapman & Hall, 1997. 525 p. v. 1.

[21] Yu A, Standish N. A study of particle size distributions. Powder Technology. 1990; 62(2):101-118.

[22] Limpert E, Stahel W, Abbt M. Log-normal distributions across the sciences: keys and clues. BioScience. 2001; 51(5):341-252.

[23] Ferrari J, Castilhos F, Araújo P, Sayer C. Modeling particle size distribution in heterogeneous polymerization systems using multimodal log-normal function. Brazilian Journal of Chemical Engineering. 2016; 33(3):469-478.

[24] Brosseau L, Fang C, Snyder C, Cohen B. Particle size distribution of automobile paint sprays. Applied Occupational and Environmental Hygiene. 1992; 7(9):607-612.

[25] Brittain H G. Solid-state analysis. In: Ahuja S, Scypinski S, editors. Handbook of Modern Pharmaceutical Analysis. Elsevier; 2001. p. 57-84.

[26] Desmond K W, Weeks E R. Influence of particle size distribution on random close packing of spheres. Physical Review E. 2014; 90(2):022204.

[27] Polakowski C, Sochan A, Bieganowski A, Ryzak M, Földényi R, Tóth J. Influence of the sand particle shape on particle size distribution measured by laser diffraction method. International Agrophysics. 2014; 28(2):195-200.

[28] Adi H, Larson I, Stewart P. Use of milling and wet sieving to produce narrow particle size distributions of lactose monohydrate in the sub-sieve range. Powder Technology. 2007; 179(1-2):95-99.

[29] Hopkins K, Weeks D. Tests for normality and measures of skewness and kurtosis: Their Place in Research Reporting. Educational and Psychological Measurement. 1990; 50(4):717-729.

[30] Blanca M, Arnau J, López-Montiel D, Bono R, Bendayan R. Skewness and kurtosis in real data samples. Methodology. 2013; 9(2):78-84.

[31] DeCarlo L. On the meaning and use of kurtosis. Psychological Methods. 1997; 2(3):292-307.

[32] Andreasen A H. Ueber die beziehung zwischen kornabstufung und zwischenraum in Produkten aus Losen Körnern (MIT Einigen Experimenten). Kolloid-Zeitschrift. 1930;50(3):217–28.

[33] Furnas C C. Grading aggregates - I. - Mathematical relations for beds of broken solids of maximum density. Industrial & Engineering Chemistry. 1931;23(9):1052–1058.

[34] Fuller W B, Thompson SE. The Laws of Proportioning Concrete. Proc. Am. Soc. Civil Engr. 1907; 33, 261.

[35] Funk J E, Dinger D R. Predictive process control of crowded particulate suspensions applied to ceramic manufacturing. New York, NY: Springer; 1994.

[36] Rosin P, Rammler E. The laws governing the fineness of powdered coal. J. Inst. Fuel. 1933; 7: 29-36.

[37] Vesilind P A. The Rosin-Rammler Particle Size Distribution. Resource Recovery and Conservation. 1980;5(3):275–7.

[38] Weibull W. A statistical distribution function of wide applicability. Journal of Applied Mechanics. 1951;18(3):293–7.

[39] Lai, C D. Generalized Weibull Distributions. 1. ed. [S. l.]: Springer, 2014. 118 p. (Springer Briefs in Statistics).

[40] Rinne, Horst. The Weibull distribution: A handbook. 1. ed. Boca Raton: CRC Press, 2009. 808 p.

[41] Murthy D N P; Xie M; Jiang R. Weibull Models. 1. ed. [S. l.]: Wiley, 2004. 408 p. (Wiley Series in Probability and Statistics).

[42] Maron S H, Pierce P E. Application of ree-eyring generalized flow theory to suspensions of spherical particles. Journal of Colloid Science. 1956;11(1):80–95.

[43] Kitano T, Kataoka T, Shirota T. An empirical equation of the relative viscosity of polymer melts filled with various inorganic fillers. Rheologica Acta. 1981;20(2):207–9.

[44] Quemada D. Rheology of concentrated disperse systems II. A model for non-Newtonian shear viscosity in steady flows. Rheologica Acta. 1978;17(6):632–42.

[45] Krieger I M, Dougherty T J. A mechanism for non-Newtonian flow in suspensions of rigid spheres. Transactions of the Society of Rheology. 1959;3(1):137–52.

[46] Coussot P. Introduction to the rheology of complex fluids. In: Roussel N, editor. Understanding the Rheology of Concrete. Woodhead Publishing; 2012; 3–22.

[47] Xu N, Blawzdziewicz J, O'Hern C S. Random close packing revisited: Ways to pack frictionless disks. Physical Review E. 2005;71(6).

[48] Manuel J G F, Bombard A J F, Weeks E R. Effect of polydispersity in concentrated magnetorheological fluids. Smart Materials and Structures. 2023;32(4):045014.

[49] Crawford T W. Scale analytical. International Encyclopedia of Human Geography. 2009;29–36.

[50] Roman S, Bertolotti F. A master equation for power laws. Royal Society Open Science. 2022;9(12).

[51] Newman M E J. Power laws, pareto distributions and Zipf's law. Contemporary Physics. 2005;46(5):323–51.

[52] Forbes C; Evans M; Hastings N; Peacock B. Statistical Distributions. 4. ed. Hoboken: John Wiley & Sons, Inc., 2011. 212 p.

[53] Bashir S, Khan H. Characterization of the weighted power function distribution by reliability functions and moments. Research in Mathematics. 2023;10(1).

[54] Brown J H, Gupta V K, Li B-L, Milne B T, Restrepo C, West G B. The fractal nature of Nature: Power laws, ecological complexity and biodiversity. Philosophical Transactions of the Royal Society of London Series B: Biological Sciences. 2002;357(1421):619–26.

[55] Tokmachev MS. Modeling of truncated probability distributions. IOP Conference Series: Materials Science and Engineering. 2018;441.

[56] Fréchet M. Sur la loi de Probabilité de l'écart Maximum. Annales de la Société Polonaise de Mathematique. 1927; 6, 93-116.

[57] Fang Z, Patterson B R, Turner M E. Modeling particle size distributions by the Weibull distribution function. Materials Characterization. 1993; 31(3):177–82.

[58] Tenchov B G, Yanev T K. Weibull distribution of particle sizes obtained by uniform random fragmentation. Journal of Colloid and Interface Science. 1986;111(1):1–7.

[59] Brouwers H J. Packing fraction of particles with a Weibull size distribution. Physical Review E. 2016; 94(1):012905.

[60] Soppe W. Computer simulation of random packings of hard spheres. Powder Technology. 1990;62(2):189–96.

[61] Zinchenko A Z. Algorithm for random close packing of spheres with periodic boundary conditions. Journal of Computational Physics. 1994;114(2):298–307.

[62] Nolan G T, Kavanagh P E. Computer simulation of random packing of hard spheres. Powder Technology. 1992;72(2):149–55.

[63] Farr R S, Groot R D. Close packing density of polydisperse hard spheres. The Journal of Chemical Physics. 2009;131(24).

[64] Farr R S. Random close packing fractions of log-normal distributions of hard spheres. Powder Technology. 2013;245:28–34.

[65] Cormen T H, Leiserson C E, Rivest R L, Stein C. Introduction to algorithms. 3rd ed. Cambridge, MA: MIT Press; 2009.

[66] Gupta S C. Delta function. IEEE Transactions on Education. 1964;E-7(1):16–22.

[67] Desmond KW, Weeks ER. Random close packing of disks and spheres in confined geometries. Physical Review E. 2009;80(5).

[68] Oquendo-Patiño W F, Estrada N. Densest arrangement of frictionless polydisperse sphere packings with a power-law grain size distribution. Granular Matter. 2020;22(4).

[69] Monti J M, Clemmer J T, Srivastava I, Silbert L E, Grest G S, Lechman J B. Large-scale frictionless jamming with power-law particle size distributions. Physical Review E. 2022;106(3).

[70] Ahsanullah M; Kibria B M G; Shakil M. Normal Distribution. In: Ahsanullah M, Kibria BMG, Shakil M, editors. Normal and Student´s t distributions and their applications. 1. ed. Paris: Atlantis Press, 2014. p. 7-50. (Atlantis Studies in Probability and Statistics, vol. 4).

[71] Patel J K; Read C B. Handbook of the Normal Distribution. 2. ed. [S. l.]: CRC Press, 1996. 456 p. (Statistics: A Series of Textbooks and Monographs, vol.150).

[72] Zuo-Wei W; Zhi-Fang L; Rui-Bao T. Influence of the Size Distribution of Particles on the Viscous Property of an Electrorheological Fluid. Chinese Physics Letters. 1997; 14:151.

[73] Crow, E L.; Shimizu, K (ed.). Log-normal distributions: theory and applications. New York: Marcel Dekker, 1988. 387 p. (Statistics: A Series of Textbooks and Monographs, v. 88).

[74] Press W H, Flannery B P, Teukolsky S A. Numerical recipes in Fortran 77: The Art of Scientific Computing. Cambridge: Cambridge University Press; 1992.

APPENDIX A – COMMON PARTICLE SIZE DISTRIBUTIONS

In the literature, several probability distributions are used to describe the variations in particle sizes. The most common choices are:

1. **Dirac delta function:**

The delta function is a mathematical object that completely describes the packing of monodisperse spheres; that is, the packing of spheres with the same diameter. From equation 29, we know it is defined as follows [66]:

$$\delta(x - x_0) = \begin{cases} \infty, & if \; x = x_0 \;, \\ 0, & if \; x \neq x_0 \;. \end{cases}$$

Therefore, a probability distribution consisting of monodisperse spheres was given by equation 30:

$$p_{3D}(D) = \delta(D - D_0) \;, \quad -\infty < D < \infty \quad ,$$

where D_0 is the mean particle size. The most important properties of the delta function are [66]:

$$\delta(x) = \delta(-x) \quad , \tag{37}$$

$$\int_{-\infty}^{\infty} \delta(x - x_0) dx = 1 \quad , \tag{38}$$

$$\int_{-\infty}^{\infty} f(x)\delta(x) dx = f(0) \text{ and } \int_{-\infty}^{\infty} f(x)\delta(x - x_0) dx = f(x_0) \quad . \tag{39}$$

In this context, the delta function is extremely important in both science and statistics since it returns the value of the function $f(x)$ at the point $x = x_0$. The Dirac delta function is illustrated in Figure 16:
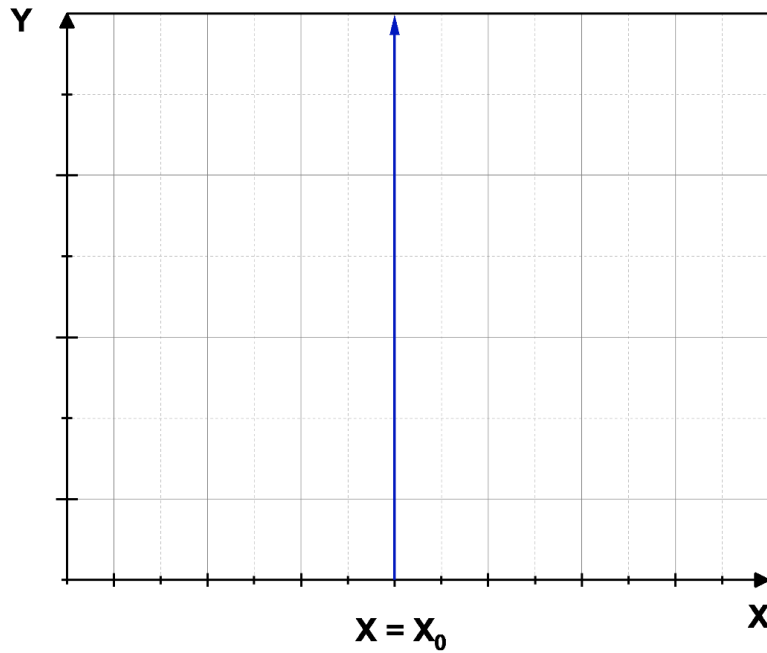
Figure 16 – The Dirac δ function is a mathematical object that is zero everywhere, except at the point $x = x_0$, where it goes to infinity. Also, the area under the "curve" is always equal to one. Source: Author, 2024.

Also, from equation 31, we know that there is an important relationship between the Dirac Delta function and the Heaviside step function [66]:

$$\theta(x - x_0) = \int_{-\infty}^{x} \delta(x' - x_0)dx' \quad .$$

And therefore:

$$\frac{d}{dx}\theta(x - x_0) = \delta(x - x_0) \qquad , \tag{40}$$

where $\theta(x - x_0)$ is the unit step function.

2. Normal distribution (gaussian):

The most important and most widely used probability distribution in all statistics, the normal distribution encompasses a family of symmetrical bell-shaped curves that differ from each other by the location parameter (μ) and the shape parameter (σ). First described by de Moivre in 1733, the normal distribution is also known as the Gaussian distribution, in honor of the German mathematician Carl Friedrich Gauss, who developed and applied this function to study the motion of celestial bodies [52, 70, 71]. An example is illustrated in Figure 17:
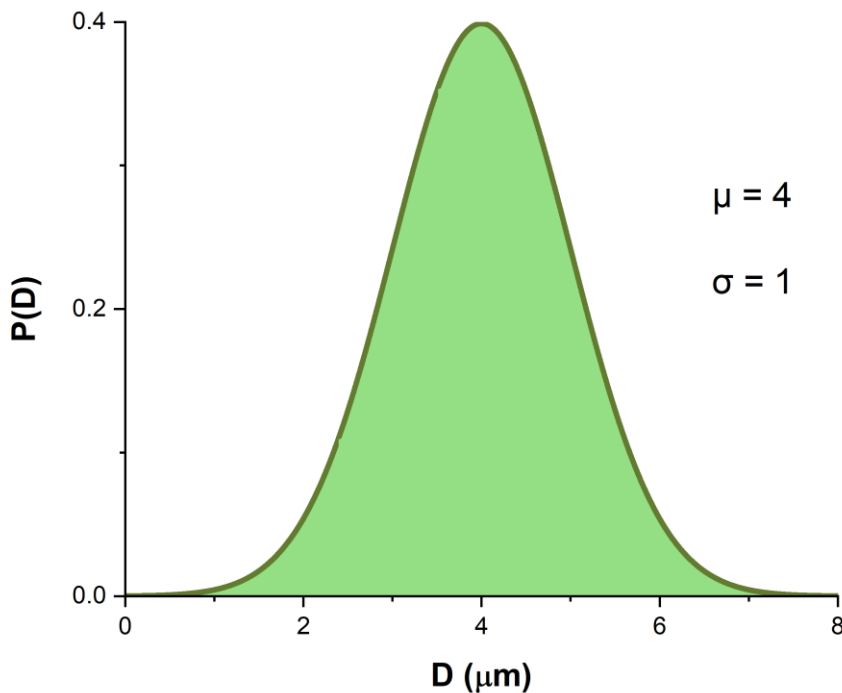
Figure 17 - A normal distribution centered at $\mu = 4$ with $\sigma = 1$. Source: Author, 2024.

The Gaussian distribution appears in a wide range of phenomena across science and mathematics [70, 71] and is sometimes used to describe the polydispersity of particulate materials, especially when we have narrower ranges of sizes [20, 72]. The main properties of this distribution are expressed in Table 20 [52, 70, 71]:

Table 20 – Properties of a normal distribution

Parameters	Random Variable X, Mean (μ) and Standard Deviation (σ)
Range	$-\infty < X < \infty;\ \sigma > 0$
PDF	$f(x) = \dfrac{1}{\sigma\sqrt{2\pi}}\,exp\left(-\dfrac{1}{2\sigma^2}(\mathrm{X}-\mu)^2\right)$
Mean	$E(X) = \mu$
Mode	$Mode(X) = \mu$
Median	$Med(X) = \mu$
Variance	$Var(X) = \sigma^2$
Coefficient of Variation (Polydispersity Index)	$\alpha = \sigma/\mu$
Skewness	$S = 0$
Kurtosis	$K = 3$

3. Log-normal distribution:

During the study of particulate materials, one often encounters skewed distributions, which are common when the mean values are low, strictly positive, and with wide variances. In this regard, the traditional Gaussian distribution is not able to accurately represent the data and, therefore, the use of log-normal distributions is common practice [20, 22].
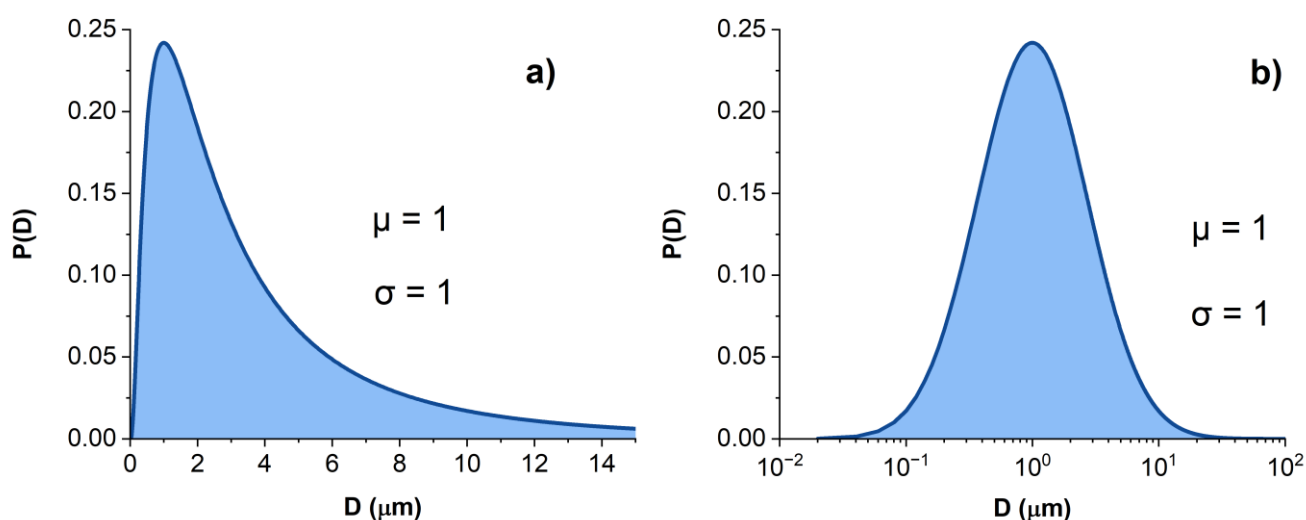
Figure 18 - A log-normal distribution in a) a linear scale and b) a logarithmic scale. Source: Author, 2024.

As one can see in Figure 18, unlike the symmetrical Gaussian distributions, log-normal distributions are asymmetric, that is, they always have $S > 0$. Its main properties are summarized in Table 21 [22, 26, 52, 73]:

Table 21 – Properties of a log-normal distribution

Parameters	Random Variable X, Mean (μ) of $\ln(X)$ and Standard Deviation (σ) of $\ln(X)$
Range	$0 < X < \infty;\ \sigma > 0$
PDF	$f(x) = \begin{cases} \dfrac{1}{X\sigma\sqrt{2\pi}}\,exp\left(-\dfrac{1}{2\sigma^2}(\ln(X) - \mu)^2\right), X > 0 \\ 0,\ X \leq 0 \end{cases}$
Mean	$E(X) = e^{\left(\mu + \frac{1}{2}\sigma^2\right)}$
Mode	$Mode(X) = e^{\left(\mu - \sigma^2\right)}$
Median	$Med(X) = e^{\mu}$
Variance	$Var(X) = e^{\left(2\mu + \sigma^2\right)}.(e^{\sigma^2} - 1)$
Coefficient of Variation (Polydispersity Index)	$\alpha = \sqrt{e^{\sigma^2} - 1}$
Skewness	$S = (e^{\sigma^2} + 2)\sqrt{e^{\sigma^2} - 1}$
Kurtosis	$K = e^{4\sigma^2} + 2e^{3\sigma^2} + 3e^{2\sigma^2} - 3$

APPENDIX B – IMPLEMENTED DISTRIBUTIONS IN RCPYTHON

This is the list of distributions currently implemented in RCPython. Note that all of them are computed using the following two steps: First, we calculate the rod distribution, as described in Farr [64]. Then, we use either an analytical or a numerical method to generate the rods according to this rod distribution, as detailed in Numerical Recipes [74]. We'll start with the simplest case where we only have one particle size distribution; that is, only one population of particles. Most of these individual distributions have a link from DESMOS for the readers to test each parameter for themselves.

1. Dirac delta function:

The delta function completely describes the packing of monodisperse spheres, that is, spheres with the same diameter. From section 3.2.1, we know that:

$$\delta(x - x_0) = \begin{cases} \infty, & if\ x = x_0 \quad, \\ 0, & if\ x \neq x_0 \quad. \end{cases}$$

And, therefore, a probability distribution of monodisperse spheres is given by:

$$p_{3D}(D) = \delta(D - D_0)\,, \quad -\infty < D < \infty \quad,$$

where D_0 is the mean size of the particles.

a) Rod distribution:

$$p_{1D}(L) = 2L \frac{\int_L^\infty \delta(D - D_0)\,dD}{\int_0^\infty \delta(D - D_0)D^2\,dD} \quad.$$

The integral from the denominator quickly reduces to:

$$p_{1D}(L) = 2L \frac{\int_L^\infty \delta(D-D_0)dD}{D_0^2} \quad .$$

But one must be extra careful with the integral on the numerator, since it goes from $[L, \infty)$, instead of $(-\infty, \infty)$. To solve this integral, we must remember that there is a well-defined relationship between the Dirac Delta function and the Heaviside step function:

$$\int_{-\infty}^{D} \delta(D'-D_0)dD' = \theta(D-D_0) \quad .$$

By taking the original integral from the delta function and splitting it in two parts, we get:

$$\int_{-\infty}^{\infty} \delta(D-D_0)dD = \int_{-\infty}^{L} \delta(D-D_0)dD + \int_L^\infty \delta(D-D_0)dD \quad ,$$

and:

$$1 = \theta(L-D_0) + \int_L^\infty \delta(D-D_0)dD \quad .$$

Therefore:

$$\int_L^\infty \delta(D-D_0)dD = 1 - \theta(L-D_0) \quad .$$

The Heaviside step function has an important identity:

$$\theta(x-x_0) + \theta(x_0-x) = 1 \quad .$$

Therefore:

$$\int_L^\infty \delta(D - D_0)dD = \theta(D_0 - L) \ ,$$

and we finally get:

$$p_{1D}(L) = \frac{2L}{D_0^2}\theta(D_0 - L) = \begin{cases} \frac{2L}{D_0^2}, & if \ L \leq D_0 \ , \\ 0, & if \ L > D_0 \ . \end{cases}$$

b) Cumulative distribution:

$$F(L) = \int_0^L p_{1D}(L')dL' \ .$$

Since the function above is defined piecewise, we have:

$$F(L) = \begin{cases} \int_0^L \frac{2L'}{D_0^2}dL', & if \ L \leq D_0 \ , \\ 0, & if \ L > D_0 \ , \end{cases}$$

and therefore:

$$F(L) = \begin{cases} \left(\frac{L}{D_0}\right)^2, & if \ L \leq D_0 \ , \\ 0, & if \ L > D_0 \ . \end{cases}$$

The inverse of $F(L)$ was then implemented numerically in Python via binary search.

2. Log-normal distribution:

The most common distribution in particle size analysis, the log-normal distribution has density defined as follows:

$$p_{3D}(D) = \frac{1}{D\sigma\sqrt{2\pi}} \exp\left\{-\frac{[ln(D/D_0)]^2}{2\sigma^2}\right\}, \quad 0 < D < \infty; \ \mu > 0; \ \sigma > 0 \ ,$$

where D_0 is the mean size of the logarithm of the diameters and σ is the standard deviation of the logarithm of the diameters.

a) Rod distribution:

$$p_{1D}(L) = 2L \frac{\int_L^\infty \frac{1}{D\sigma\sqrt{2\pi}} \exp\left\{-\frac{[ln(D/D_0)]^2}{2\sigma^2}\right\} dD}{\int_0^\infty \frac{D}{\sigma\sqrt{2\pi}} \exp\left\{-\frac{[ln(D/D_0)]^2}{2\sigma^2}\right\} dD} \ .$$

To solve this expression, note that the denominator of $p_{1D}(L)$ is the second raw moment of the log-normal distribution, that is [52, 64, 73]:

$$E[X^2] = Var[X] + E^2[X] = \int_0^\infty \frac{D}{\sigma\sqrt{2\pi}} \exp\left\{-\frac{[ln(D/D_0)]^2}{2\sigma^2}\right\} dD = D_0^2 \exp(2\sigma^2) \ .$$

Therefore:

$$p_{1D}(L) = 2L \frac{\int_L^\infty \frac{1}{D\sigma\sqrt{2\pi}} \exp\left\{-\frac{[ln(D/D_0)]^2}{2\sigma^2}\right\} dD}{D_0^2 \exp(2\sigma^2)} \ .$$

Reorganizing the exponential, we get:

$$p_{1D}(L) = \frac{2L}{D_0^2 \exp(2\sigma^2)} \int_L^\infty \frac{1}{D\sigma\sqrt{2\pi}} \exp\left\{-\left(\frac{\ln(D/D_0)}{\sigma\sqrt{2}}\right)^2\right\} dD \ .$$

Since $erfc(x) = \frac{2}{\sqrt{\pi}} \int_x^{\infty} e^{-t^2} dt$, we factor out $1/\sqrt{\pi}$:

$$p_{1D}(L) = \frac{2L}{D_0^2 \exp(2\sigma^2)} \frac{1}{\sqrt{\pi}} \int_L^{\infty} \frac{1}{D\sigma\sqrt{2}} \exp\left\{-\left(\frac{\ln(D/D_0)}{\sigma\sqrt{2}}\right)^2\right\} dD \quad .$$

Then, we let $u = \frac{\ln(D/D_0)}{\sigma\sqrt{2}}$ and $du = \frac{1}{D\sigma\sqrt{2}} dD$:

$$p_{1D}(L) = \frac{L}{D_0^2 \exp(2\sigma^2)} \frac{2}{\sqrt{\pi}} \int_L^{\infty} \exp\{-u^2\} du \quad .$$

and we can clearly see that:

$$p_{1D}(L) = \frac{L \exp(-2\sigma^2)}{D_0^2} erfc\left[\frac{\ln(L/D_0)}{\sigma\sqrt{2}}\right] \quad .$$

b) Cumulative Distribution:

$$F(L) = \int_0^L p_{1D}(L')dL' = \int_0^L \frac{L' \exp(-2\sigma^2)}{D_0^2} erfc\left[\frac{\ln(L'/D_0)}{\sigma\sqrt{2}}\right] dL' \quad .$$

Using identity 25 from Farr [64], we know that:

$$Var(D)F(L) = L^2 \int_L^{\infty} p_{3D}(D)dD + \int_0^L p_{3D}(D)D^2 dD \quad ,$$

and therefore:

$$F(L) = \frac{L^2 \int_L^{\infty} p_{3D}(D)dD}{Var(D)} + \frac{\int_0^L p_{3D}(D)D^2 dD}{Var(D)} \quad ,$$

$$F(L) = \frac{L^2 \int_L^{\infty} p_{3D}(D)dD}{D_0^2 \exp(2\sigma^2)} + \frac{\int_0^L p_{3D}(D)D^2 dD}{D_0^2 \exp(2\sigma^2)} \quad .$$

The integral on the left is easier to solve:

$$F(L) = \frac{L^2}{D_0^2 \exp{(2\sigma^2)}}\left[1 - \frac{1}{2}erfc\left(-\frac{\ln(L/D_0)}{\sigma\sqrt{2}}\right)\right] + \frac{\int_0^L p_{3D}(D)D^2 dD}{D_0^2 \exp{(2\sigma^2)}} \quad,$$

and we get:

$$F(L) = \frac{L^2 \exp{(-2\sigma^2)}}{2D_0^2} erfc\left[\frac{\ln(L/D_0)}{\sigma\sqrt{2}}\right] + \frac{\int_0^L p_{3D}(D)D^2 dD}{D_0^2 \exp{(2\sigma^2)}} \quad.$$

The integral on the right side is trickier. However, from Farr [64], equation 20, we know that:

$$I_n(L) = \int_L^\infty D^n \exp\left\{-\left(\frac{\ln(D/D_0)}{\sigma\sqrt{2}}\right)^2\right\}dD = D_0^{n+1}\sigma\sqrt{\frac{\pi}{2}}\, e^{[(n+1)^2\sigma^2/2]}\, erfc\left[\frac{\ln(L/D_0)}{\sigma\sqrt{2}} - \frac{(n+1)\sigma}{\sqrt{2}}\right] \quad.$$

Therefore:

$$F(L) = \frac{L^2 \exp{(-2\sigma^2)}}{2D_0^2} erfc\left[\frac{\ln(L/D_0)}{\sigma\sqrt{2}}\right] + \frac{1}{D_0^2 \exp{(2\sigma^2)}}\left[Var(D) - \frac{1}{\sigma\sqrt{2\pi}}I_1(L)\right] \quad,$$

$$F(L) = \frac{L^2 \exp{(-2\sigma^2)}}{2D_0^2} erfc\left[\frac{\ln(L/D_0)}{\sigma\sqrt{2}}\right] + \frac{1}{D_0^2 \exp{(2\sigma^2)}}\left[D_0^2 \exp{(2\sigma^2)} - \frac{1}{\sigma\sqrt{2\pi}}I_1(L)\right] \quad.$$

And finally:

$$F(L) = \frac{L^2 \exp(-2\sigma^2)}{2D_0^2} erfc\left[\frac{\ln(L/D_0)}{\sigma\sqrt{2}}\right] + 1 - \frac{1}{2}erfc\left[\frac{\ln(L/D_0)}{\sigma\sqrt{2}} - \frac{2\sigma}{\sqrt{2}}\right] \quad.$$

The inverse of $F(L)$ was then implemented numerically using binary search.

DESMOS → https://www.desmos.com/calculator/gzh8itolth?lang=pt-BR

3. Weibull distribution:

The Weibull distribution is one of the most powerful tools in reliability analysis and can also be utilized to model particle size distributions. In its most basic form, the Weibull distribution has only one parameter, as follows:

$$p(D) = cD^{c-1} \exp\{-D^c\} \ , \quad 0 \le D < \infty \, ; \ \ c > 0 \quad .$$

However, we want to implement the more general, three-parameter version of the Weibull distribution, which is defined as:

$$p_{3D}(D) = \frac{c}{b}\left(\frac{D-a}{b}\right)^{c-1} \exp\left\{-\left(\frac{D-a}{b}\right)^c\right\}, \ \ a \le D < \infty \, ; \ \ a, \ b, \ c > 0 \quad ,$$

where c is the shape parameter, b is the scale parameter, and a is the location parameter. To "convert" the one-parameter Weibull into its number-weighted three-parameter form, we can perform a location-scale transformation:

$$p_{3D}(D) = \frac{1}{b} p\left(\frac{D-a}{b}\right) \quad .$$

From the formula above, we get:

$$cD^{c-1}\exp\{-D^c\} \ \xrightarrow{\ location-scale\ } \ \frac{c}{b}\left(\frac{D-a}{b}\right)^{c-1}\exp\left\{-\left(\frac{D-a}{b}\right)^c\right\} \quad .$$

This same reasoning will be used to compute the rod distribution: first we will calculate the one-parameter rod distribution and then a location-scale transformation will be performed to obtain the three-parameter rod distribution.

a) Rod distribution:

As stated before, the one-parameter Weibull is given by:

$$p(D) = cD^{c-1} \exp\{-D^c\} , \quad 0 \leq D < \infty; \quad c > 0 .$$

Thus, its rod distribution is:

$$p_{1D}(L) = 2L \frac{\int_L^\infty cD^{c-1} \exp\{-D^c\} \; dD}{\int_0^\infty cD^{c+1} \exp\{-D^c\} \; dD} .$$

To solve this expression, we first note that the denominator of $p_{1D}(L)$ is the second raw moment of the one-parameter Weibull, that is [39, 52, 64]:

$$E[X^2] = Var[X] + E^2[X] = \int_0^\infty cD^{c+1} \exp\{-D^c\} \; dD = \Gamma\left(1 + \frac{2}{c}\right) .$$

Therefore:

$$p_{1D}(L) = 2L \frac{\int_L^\infty cD^{c-1} \exp\{-D^c\} \; dD}{\Gamma\left(1 + \frac{2}{c}\right)} .$$

To solve the integral at the numerator, we let $u = D^c$ and $du = cD^{c-1}dD$. Then:

$$\int_L^\infty \exp\{-u\} \, du = |- \exp[-u]|_L^\infty .$$

Substituting back the original values, we get:

$$\int_L^\infty cD^{c-1} \exp\{-D^c\} \; dD = |- \exp[-D^c]|_L^\infty = \exp[-L^c] .$$

And finally:

$$p_{1D}(L) = 2L \frac{\exp[-L^c]}{\Gamma\left(1 + \frac{2}{c}\right)} \quad.$$

Now, we can use the location-scale transformation to get our three-parameter rod distribution:

$$2L \frac{\exp[-L^c]}{\Gamma\left(1 + \frac{2}{c}\right)} \xrightarrow{\ location-scale\ } \underbrace{\frac{2\left(\frac{L-a}{b}\right)\exp\left[-\left(\frac{L-a}{b}\right)^c\right]}{b\Gamma\left(1 + \frac{2}{c}\right)}}_{Three-Parameter\ Rod\ Distribution} \quad.$$

b) Cumulative Distribution:

$$F(L) = \int_a^L p_{1D}(L')dL' = \int_a^L \frac{2\left(\frac{L'-a}{b}\right)\exp\left[-\left(\frac{L'-a}{b}\right)^c\right]}{b\Gamma\left(1 + \frac{2}{c}\right)} dL' \quad,$$

$$F(L) = \frac{2\int_a^L \left(\frac{L'-a}{b}\right)\exp\left[-\left(\frac{L'-a}{b}\right)^c\right] dL'}{b\Gamma\left(1 + \frac{2}{c}\right)} \quad.$$

The integral in the numerator is not straightforward to solve. However, we can implement both $F(L)$ and its inverse numerically. This was done with the help of SciPy, a scientific computing library from Python.

DESMOS → https://www.desmos.com/calculator/ts5hmopqqd?lang=pt-BR

4. Andreasen-Andersen Distribution (Power Law):

As described in section 4.1, the Andreasen-Andersen distribution is a volume-weighted power law with probability density function:

$$p_{3D}(D) = q \cdot \frac{D^{q-1}}{D_{max}^q} \qquad 0 \leq D \leq D_{max}; \quad q > 0; \ D_{max} > 0 \quad ,$$

where D_{max} is the maximum particle size and q is the exponent of the distribution, the so-called distribution modulus. To calculate its rod distribution, however, we first need to convert $p_{3D}(D)$ into a number-weighted distribution. Recall from equation 5 that:

$$q_r(D) = \frac{D^{r-t}}{\int_{D_{min}}^{D_{max}} D^{r-t} q_t(D) dD} \ q_t(D) \ ,$$

where q_t is our original probability distribution and q_r is our converted distribution. Setting $r = 0$ and $t = 3$, we can get our number-weighted Andreasen-Andersen model:

$$p_{3D\ Number}(D) = (q - 3) \cdot \frac{D^{q-4}}{D_{max}^{q-3}} \qquad 0 \leq D \leq D_{max}; \quad q > 3; \ D_{max} > 0 \quad .$$

This is the function that will be used to compute the rod distribution.

a) Rod distribution:

Since the support of the Andreasen-Andersen model is truncated at $[0, D_{max}]$, the rod distribution is calculated in a slightly different way:

$$p_{1D}(L) = 2L \frac{\int_L^{D_{max}} (q-3) \cdot \frac{D^{q-4}}{D_{max}^{q-3}} dD}{\int_0^{D_{max}} (q-3) \cdot \frac{D^{q-4}}{D_{max}^{q-3}} D^2 dD} \quad .$$

We can cancel out the constants to get:

$$p_{1D}(L) = 2L \frac{\int_L^{D_{max}} D^{q-4} dD}{\int_0^{D_{max}} D^{q-2} dD} \quad ,$$

and the expression quickly reduces to:

$$p_{1D}(L) = 2L \frac{\left|\frac{D^{q-3}}{q-3}\right|_L^{D_{max}}}{\left|\frac{D^{q-1}}{q-1}\right|_0^{D_{max}}} \quad .$$

Therefore:

$$p_{1D}(L) = 2L \frac{(q-1)}{(q-3)} \frac{(D_{max}^{q-3} - L^{q-3})}{(D_{max}^{q-1})} \qquad 0 \leq L \leq D_{max}; \quad q > 1; \quad D_{max} > 0 \quad .$$

b) Cumulative Distribution:

$$F(L) = \int_0^L p_{1D}(L') dL' = \int_0^L 2L' \frac{(q-1)}{(q-3)} \frac{(D_{max}^{q-3} - L'^{q-3})}{(D_{max}^{q-1})} dL' \quad .$$

Factoring out the constants, we get:

$$F(L) = \frac{2(q-1)}{D_{max}^{q-1}(q-3)} \int_0^L L' \left(D_{max}^{q-3} - L'^{q-3}\right) dL' \quad ,$$

$$F(L) = \frac{2(q-1)}{D_{max}^{q-1}(q-3)} \left[\int_0^L D_{max}^{q-3} L' dL' - \int_0^L L'^{q-2} dL' \right] \quad .$$

These integrals are straightforward to solve:

$$F(L) = \frac{2(q-1)}{D_{max}^{q-1}(q-3)}\left[\frac{D_{max}^{q-3}L^2}{2} - \frac{L^{q-1}}{q-1}\right] \quad 0 \le L \le D_{max}; \quad q > 1; \quad D_{max} > 0 .$$

Finally, to completely describe the behavior of the Andreasen-Andersen distribution, the exponent q must be greater than zero. Therefore, $p_{1D}(L)$ and $F(L)$ need to be displaced one unit to the left. By substituting $k = q - 1$, we get:

$$p_{1D}(L_k) = 2L_k\frac{k}{k-2}\frac{(D_{max}^{k-2} - L_k^{k-2})}{(D_{max}^k)} \quad 0 \le L \le D_{max}; \quad k > 0; \quad D_{max} > 0 ,$$

$$F(L_k) = \frac{2k}{D_{max}^k(k-2)}\left[\frac{D_{max}^{k-2}L_k^2}{2} - \frac{L_k^k}{k}\right] \quad 0 \le L \le D_{max}; \quad k > 0; \quad D_{max} > 0 .$$

The inverse of $F(L_k)$ was then implemented numerically using binary search.

DESMOS → https://www.desmos.com/calculator/tqayxjrrpe?lang=pt-BR

5. Dinger-Funk Distribution (Doubly Truncated Power Law):

As described in section 4.2, the Dinger-Funk distribution is a power law doubly truncated in the interval $[D_{min}, D_{max}]$ and with probability density function given by:

$$p_{3D}(D) = q \cdot \frac{D^{q-1}}{D_{max}^q - D_{min}^q} \qquad D_{min} \leq D \leq D_{max}; \quad q \neq 0, \; D_{min}, D_{max} > 0 \;,$$

where D_{min} is the minimum particle size, D_{max} is the maximum particle size and q is the exponent of the distribution, called distribution modulus.

Since the Dinger-Funk distribution is a truncated version of the Andreasen-Andersen distribution, then the Dinger-Funk rod distribution will also be a truncated version of the Andreasen-Andersen rod distribution. In other words, by truncating the following expression:

$$p_{1D}(L) = 2L \frac{(q-1)}{(q-3)} \frac{(D_{max}^{q-3} - L^{q-3})}{(D_{max}^{q-1})} \;, \qquad 0 \leq L \leq D_{max}; \quad q > 1; \; D_{max} > 0 \;.$$

We can compute the Dinger-Funk rod distribution.

a) Rod distribution:

Recall from equation 17 that a doubly truncated probability distribution is defined as follows:

$$t(D) = \frac{p(D)}{\int_{D_{min}}^{D_{max}} p(D) \, dD} \;, \qquad D_{min} \leq D \leq D_{max}, \; D_{min} > 0, \; D_{max} > D_{min} \;.$$

Therefore, the truncated Andreasen-Andersen rod distribution is:

$$p_{1D}(L) = \frac{2L \dfrac{(q-1)}{(q-3)} \dfrac{(D_{max}^{q-3} - L^{q-3})}{(D_{max}^{q-1})}}{\int_{D_{min}}^{D_{max}} 2L \dfrac{(q-1)}{(q-3)} \dfrac{(D_{max}^{q-3} - L^{q-3})}{(D_{max}^{q-1})} \, dL} \;.$$

Cancelling the constants, we get:

$$p_{1D}(L) = \frac{L(D_{max}^{q-3} - L^{q-3})}{\int_{D_{min}}^{D_{max}} L(D_{max}^{q-3} - L^{q-3})dL} \quad.$$

The integral in the denominator is straightforward to solve and quickly becomes:

$$p_{1D}(L) = \frac{L(D_{max}^{q-3} - L^{q-3})}{\dfrac{D_{max}^{q-3}}{2}(D_{max}^2 - D_{min}^2) - \dfrac{1}{q-1}\left(D_{max}^{q-1} - D_{min}^{q-1}\right)} \quad.$$

b) Cumulative Distribution:

Integrating the previous function, we get:

$$F(L) = \int_{D_{min}}^{L} \left[\frac{L\left(D_{max}^{q-3} - L^{q-3}\right)}{[D_{max}^{q-3}\left(D_{max}^2 - D_{min}^2\right)/2] - [\left(D_{max}^{q-1} - D_{min}^{q-1}\right)/q - 1]}\right] dL \quad.$$

By factoring out the constants, we get:

$$F(L) = \frac{\int_{D_{min}}^{L} L\left(D_{max}^{q-3} - L^{q-3}\right)dL}{[D_{max}^{q-3}\left(D_{max}^2 - D_{min}^2\right)/2] - [\left(D_{max}^{q-1} - D_{min}^{q-1}\right)/q - 1]} \quad.$$

The integral on the numerator is easily solvable and yields:

$$F(L) = \frac{\left[D_{max}^{q-3}\left(L^2 - D_{min}^2\right)/2\right] - [\left(L^{q-1} - D_{min}^{q-1}\right)/q - 1]}{[D_{max}^{q-3}\left(D_{max}^2 - D_{min}^2\right)/2] - [\left(D_{max}^{q-1} - D_{min}^{q-1}\right)/q - 1]} \quad.$$

The inverse of $F(L)$ was then implemented numerically using binary search.

DESMOS → https://www.desmos.com/calculator/f3wobdezh5?lang=pt-BR

Now, we can start computing the packing fractions of mixtures of different populations of particles. According to Farr [64], any mixture of distributions can be decomposed into a sum of "simpler" distributions following the equation:

$$p_{3D}(D) = \sum_i a_i p_i(D) \ ,$$

where p_i is the i-th distribution and a_i are fractions of the total number of particles such that $\sum_i a_i = 1$, that is, they are the weights of each population of particles. The process is extremely similar to the cases where we had only one population of particles. Also, the weights guarantee that the resulting distribution is normalized.

Note, however, that it is difficult to know the exact number of particles in each population, so the easiest way to compute the packings is by using the occluded volume of each population. Recall from equation 27 that the occluded volume is the total volume occupied by the particles when they are submerged in a liquid where they are insoluble, that is:

$$v_i = \frac{m_i}{\rho_i} \ ,$$

where m_i is the mass of a given population of particles and ρ_i is the density of this population.

With that in mind, the weights of each population of particles can be calculated as:

$$a_i = \left(\frac{v_i}{\mu_{3,i}} \right) \left[\sum_j \left(\frac{v_j}{\mu_{3,i}} \right) \right]^{-1} \ ,$$

where $\mu_{3,i} = \int_0^\infty p_i D^3 dD$ is the third raw moment of the i-th number-weighted size distribution.

So far, RCPython can compute mixtures of the following functions:

1. Dirac delta functions:

Assuming the distribution of interest is composed by a sum of delta functions, we have:

$$p_{3D}(D) = \sum_i a_i \delta(D - D_i) = a_1 \delta(D - D_1) + a_2 \delta(D - D_2) + a_3 \delta(D - D_3) + \cdots + a_n \delta(D - D_n) \,.$$

Then, the weights of the distributions can be calculated as [64]:

$$a_i = \left(\frac{v_i}{D_i^3}\right)\left[\sum_j \left(\frac{v_j}{D_j^3}\right)\right]^{-1} \,.$$

Now, we can perform the calculations of the rod distribution:

a) Rod distribution:

$$p_{1D}(L) = 2L \frac{\int_L^\infty [a_1 \delta(D - D_1) + a_2 \delta(D - D_2) + a_3 \delta(D - D_3) + \cdots + a_n \delta(D - D_n)]dD}{\int_0^\infty [a_1 \delta(D - D_1) + a_2 \delta(D - D_2) + a_3 \delta(D - D_3) + \cdots + a_n \delta(D - D_n)]D^2 dD} \,.$$

We already know that $\int_L^\infty \delta(D - D_0)dD = \theta(D_0 - L)$. Therefore:

$$p_{1D}(L) = 2L \frac{\sum_i a_i \, \theta(D_i - L)}{\sum_i a_i D_i^2} \,,$$

where $\theta(D_0 - L)$ is the Heaviside step function.

b) Cumulative Distribution:

$$F(L) = \int_0^L p_{1D}(L')dL' \quad,$$

$$F(L) = \int_0^L 2L' \frac{\sum_i a_i \theta(D_i - L')}{\sum_i a_i D_i^2} dL' \quad,$$

$$F(L) = \frac{\left[\sum_{i:D_i \leq L} a_i D_i^2 + \sum_{i:D_i > L} a_i L^2 \right]}{\sum_i a_i D_i^2} \quad.$$

The inverse of $F(L)$ was then implemented numerically via binary search. Note that this method follows the same reasoning as the one described in section 5.1.4.

2. Log-normal distributions:

Assuming the distribution of interest is composed by a sum of number-weighted log-normal distributions and that we know the values of $D_{4,3}$ and $D_{3,2}$ for each population, then [64]:

$$p_{3D}(D) = \sum_i \frac{a_i}{D\sigma_i \sqrt{2\pi}} \exp\left\{ -\left[\frac{ln\left(e^{7\sigma_i^2/2}D/D_{4,3;i}\right)}{\sigma_i \sqrt{2}} \right]^2 \right\} \quad,$$

where:

$$a_i = \left(\frac{v_i}{(D_{4,3;i})^3 e^{-6\sigma_i^2}} \right) \left[\sum_j \left(\frac{v_j}{(D_{4,3;j})^3 e^{-6\sigma_j^2}} \right) \right]^{-1} \quad,$$

and:

$$\sigma_i = \sqrt{\ln\left(\frac{D_{4,3;i}}{D_{3,2;i}}\right)} \quad .$$

Therefore, the rod distribution and its cumulative function are given by:

a) Rod distribution:

$$p_{1D}(L) = 2L \frac{\int_L^\infty \left[\sum_i \frac{a_i}{D\sigma_i\sqrt{2\pi}}\exp\left\{-\left[\ln\left(e^{7\sigma_i^2/2}D/D_{4,3;i}\right)/\sigma_i\sqrt{2}\right]^2\right\}\right]dD}{\int_0^\infty \left[\sum_i \frac{a_i}{D\sigma_i\sqrt{2\pi}}\exp\left\{-\left[\ln\left(e^{7\sigma_i^2/2}D/D_{4,3;i}\right)/\sigma_i\sqrt{2}\right]^2\right\}\right]D^2\,dD} \quad .$$

Setting $u = \ln\left(e^{7\sigma_i^2/2}D/D_{4,3;i}\right)/\sigma_i\sqrt{2}$ and $du = dD/\sigma_i\sqrt{2}$, we get:

$$p_{1D}(L) = 2L \frac{\sum_i\left\{\frac{a_i}{2}\,erfc\left[\ln\left(e^{7\sigma_i^2/2}L/D_{4,3;i}\right)/\sigma_i\sqrt{2}\right]\right\}}{\sum_i[a_i(D_{4,3;i})^2 e^{-5\sigma_i^2}]} \quad .$$

b) Cumulative Distribution

$$F(L) = \int_0^L p_{1D}(L')dL' \quad ,$$

$$F(L) = \int_0^L \left[2L'\frac{\sum_i\left\{\frac{a_i}{2}\,erfc\left[\ln\left(e^{7\sigma_i^2/2}L'/D_{4,3;i}\right)/\sigma_i\sqrt{2}\right]\right\}}{\sum_i[a_i(D_{4,3;i})^2 e^{-5\sigma_i^2}]}\right]dL' \quad .$$

And finally:

$$F(L) = \frac{\sum_i a_i \left[A_i \left(D_{4,3;i} \right)^2 + B_i L^2 \right]}{\sum_i a_i \left(D_{4,3;i} \right)^2 e^{-5\sigma_i^2}} \quad,$$

where:

$$A_i = \frac{e^{-5\sigma_i^2}}{2} \left\{ 2 - erfc \left[\frac{ln\left(e^{7\sigma_i^2/2} L / D_{4,3;i} \right)}{\sigma_i \sqrt{2}} - \frac{2\sigma_i}{\sqrt{2}} \right] \right\},$$

$$B_i = \frac{1}{2} erfc \left[\frac{ln\left(e^{7\sigma_i^2/2} L / D_{4,3;i} \right)}{\sigma_i \sqrt{2}} \right].$$

The inverse of $F(L)$ was then implemented numerically using binary search.